

## 5 Appendix A: Spectroscopy of *cis-cis* HOONO and the HOONO/HONO<sub>2</sub> Branching Ratio in the Reaction OH+NO<sub>2</sub>+M; Discharge Flow Studies

### 5.1 *Previously Published Results*

*This paper is reproduced with permission from the Journal of Physical Chemistry A, volume 107, no. 36, p. 6974-6985. Copyright 2003, American Chemical Society.*

## Cavity Ringdown Spectroscopy of *cis-cis* HOONO and the HOONO/HONO<sub>2</sub> Branching Ratio in the Reaction OH + NO<sub>2</sub> + M

Brian D. Bean,<sup>†</sup> Andrew K. Mollner, Sergey A. Nizkorodov,<sup>‡</sup> Gautham Nair, and Mitchio Okumura\*

*Arthur Amos Noyes Laboratory of Chemical Physics, MC 127-72, California Institute of Technology, Pasadena, California 91125*

Stanley P. Sander\*

*NASA Jet Propulsion Laboratory, MC 183-901, California Institute of Technology, Pasadena, California 91109*

Kirk A. Peterson

*Department of Chemistry, Washington State University, Pullman, Washington 99164-4630*

Joseph S. Francisco

*Department of Chemistry, Purdue University, West Lafayette, Indiana 47907A*

*Received: February 17, 2003; In Final Form: June 27, 2003*

The termolecular association reaction OH + NO<sub>2</sub> + M was studied in a low-pressure discharge flow reactor, and both HONO<sub>2</sub> and HOONO products were detected by infrared cavity ringdown spectroscopy (IR-CRDS). The absorption spectrum of the fundamental  $\nu_1$  band of the *cis-cis* isomer of HOONO (pernitrous or peroxyoxynitrous acid) was observed at 3306 cm<sup>-1</sup>, in good agreement with matrix isolation studies and ab initio predictions. The rotational contour of this band was partially resolved at 1 cm<sup>-1</sup> resolution and matched the profile predicted by ab initio calculations. The integrated absorbances of the  $\nu_1$  bands of the *cis-cis* HOONO and HONO<sub>2</sub> products were measured as a function of temperature and pressure. These were converted to product branching ratios by scaling the experimentally observed absorbances with ab initio integrated cross sections for HOONO and HONO<sub>2</sub> computed at the CCSD(T)/cc-pVTZ level. The product branching ratio for *cis-cis* HOONO to HONO<sub>2</sub> was  $0.075 \pm 0.020(2\sigma)$  at room temperature in a 20 Torr mixture of He/Ar/N<sub>2</sub> buffer gas. The largest contribution to the uncertainty is from the ab initio ratio of the absorption cross sections, computed in the double harmonic approximation, which is estimated to be accurate to within 20%. The branching ratio decreased slightly with temperature over the range 270 to 360 K at 20 Torr. Although *trans-perp* HOONO was not observed, its energy was computed at the CCSD(T)/cc-pVTZ level to be  $E_0 = +3.4$  kcal/mol relative to the *cis-cis* isomer. Statistical rate calculations showed that the conformers of HOONO should reach equilibrium on the time scale of this experiment. These results suggested that essentially all isomers had converted to *cis-cis* HOONO; thus, the reported branching ratio is a lower bound for and may represent the entire HOONO yield.

### Introduction

The free radical chain termination reaction



is important in oxidation chemistry throughout the lower atmosphere. Radicals in both the HO<sub>x</sub> and NO<sub>x</sub> families mediate the destruction of ozone in the stratosphere and are central to the formation of photochemical smog in the troposphere.<sup>1,2</sup> Reaction 1 reduces the concentrations of these species by converting them into the stable reservoir species nitric acid. The

rate of reaction 1 has important consequences for tropospheric ozone production and photochemical smog. In polluted urban airsheds with high ratios of NO<sub>x</sub> to volatile organic compounds (VOC), the rate of reaction 1 is one of the single most influential parameters determining peak ozone mixing ratios.<sup>3,4</sup> At high enough NO<sub>x</sub> levels, urban ozone levels decrease with increasing NO<sub>x</sub>, because elevated NO<sub>x</sub> levels reduce OH concentrations through reaction 1 and lead to reduced VOC oxidation rates. Tonnesen<sup>5</sup> has shown that model predictions of ozone production can be almost inversely proportional to changes in the rate coefficient for reaction 1 under these conditions. This negative feedback complicates ozone attainment strategies, which must often balance regulation of VOC vs NO<sub>x</sub> emissions. Furthermore, the uncertainty in the rate of reaction 1 is the major contribution to model uncertainties in predicted ozone at high NO<sub>x</sub> levels. This uncertainty propagates to scales such as the Maximum Incremental Reactivity, a measure of the ozone-

\* Corresponding Authors. E-mail (Okumura): mo@its.caltech.edu. E-mail (Sander): Stanley.P.Sander@jpl.nasa.gov.

<sup>†</sup> Current address: Department of Chemistry, University of Wisconsin-Madison, Madison, WI 53706.

<sup>‡</sup> Current address: Department of Chemistry, University of California at Irvine, Irvine, CA 92697.

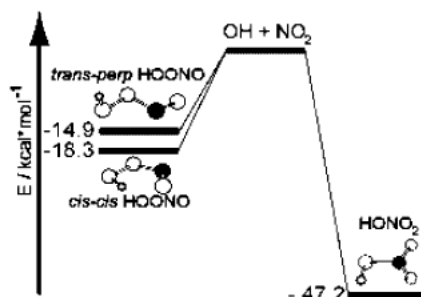


Figure 1. Energy level diagram of the reaction  $\text{OH} + \text{NO}_2$ . The *cis-cis* and *trans-perp* isomers of HOONO are shown. Energies for HOONO are from CCSD(T) calculations.

forming potential of individual VOCs.<sup>6,7</sup> In the stratosphere, both  $\text{HO}_x$  and  $\text{NO}_x$  radicals are involved in catalytic cycles that deplete ozone. Reaction 1 couples these catalytic cycles, and is one of several key reactions that lead to a more complex dependence of stratospheric ozone on  $\text{NO}_x$  levels. Sensitivity analyses have shown that differences in recommended rates for reaction 1 have a significant effect on mid-latitude ozone concentrations.<sup>8</sup>

Despite extensive studies over a wide range of temperatures and pressures,<sup>9–26</sup> significant uncertainties remain at atmospherically relevant pressures and temperatures. Much attention has recently focused on the yield for a second minor product channel



producing HOONO (peroxynitrous or pernitrous acid), a weakly bound isomer of nitric acid. The NASA Panel for Data Evaluation<sup>27</sup> and the IUPAC Gas Kinetic Data Evaluation<sup>28,29</sup> summarize the current evidence for this channel, but neither source currently makes a recommendation for its inclusion in atmospheric models. A significant branching fraction into channel 2 is of importance in the atmosphere. Formation of HOONO would reduce the efficiency of the  $\text{OH} + \text{NO}_2 + \text{M}$  reaction as a sink for OH and  $\text{NO}_2$  radicals, because HOONO would rapidly dissociate or photolyze back to reactants.

While Leighton<sup>30</sup> had suggested the existence of the HOONO channel in the gas phase, Robertshaw and Smith<sup>9</sup> first proposed that a significant HOONO yield could resolve a discrepancy in the pressure dependence of reaction 1. The effective bimolecular rate constant  $k_1$  has an anomalous falloff curve; the observed high-pressure rate constant  $k_1^\infty$  is significantly larger than the high-pressure limit extrapolated from low-pressure data. The discrepancy can be removed if the HOONO channel is insignificant at low pressures, but becomes comparable to the  $\text{HONO}_2$  channel at high pressures. Golden and Smith<sup>31</sup> modeled the  $\text{OH} + \text{NO}_2$  reaction and showed that the high- and low-pressure data could be described quantitatively by statistical models that included HOONO. Hippler et al.<sup>32</sup> have recently revised the high-pressure rate constants in He and  $\text{N}_2$  downward by  $\approx 30\%$ , but the discrepancy remains.

An energy level diagram illustrating these two channels is shown in Figure 1. At low pressures, the initial HOONO association adduct will redissociate more quickly than  $\text{HONO}_2$  due to the former's lower density of states, and bound HOONO will be formed in low yields. At high pressures, the weakly bound complex will be stabilized rapidly and the HOONO yield could be comparable to, or even exceed, the  $\text{HONO}_2$  yield.

Golden and Smith,<sup>31</sup> Matheu and Green,<sup>33</sup> and Troe<sup>34</sup> have modeled the pressure and temperature dependence of  $k_1$  and  $k_2$ . Since the submission of this paper, there has been a new set of master equation calculations by Golden, Barker, and Lohr.<sup>35</sup> While all sets of calculations suggest that HOONO formation should compete with the  $\text{HONO}_2$  channel in the reaction  $\text{OH} + \text{NO}_2$ , the resulting branching ratios at 1 atm and 298 K vary from  $>1\%$  (Matheu and Green), to 2.5% (Troe), to 30% (Golden and Smith). However, rate constants, falloff curves, and product yields cannot be calculated quantitatively from first principles, because our knowledge of the transition states, relaxation processes, and potential surfaces (especially for HOONO formation) is too limited. These models rely to some extent on fitting experimental data, and thus may not accurately predict branching ratios without direct measurements of HOONO.

There have been extensive calculations<sup>36–45</sup> of the energetics and conformations of peroxynitrous acid. From MP2 calculations, McGrath and Rowland found three stable forms of HOONO, the *cis-cis*, *cis-trans*, and *trans-perp* isomers (distinguished by the HOON and OONO torsional angles). However, recent results at the highest levels of theory (QCISD(T)/cc-pVTZ) indicate that only the *cis-cis* and *trans-perp* conformations are stable stationary points.<sup>46</sup> The best purely theoretical estimate of the O–O bond energy of *cis-cis* HOONO is  $\Delta_2 H_0 = -19.8$  kcal/mol at the CCSD(T)/CBS limit with corrections.<sup>44</sup> This estimate is based on the computed  $\Delta_f H_0^0(\text{NO}_2)$ , which is in error by 1.5 kcal/mol. A perhaps more accurate assessment, based on  $\Delta_f H_0^0(\text{cis-cis HOONO}) - \Delta_f H_0^0(\text{HONO}_2) = 29.0$  kcal/mol, gives  $\Delta_2 H_0 = -18.3$  kcal/mol. In either case, this binding energy is large enough to expect that *cis-cis* HOONO will be a relatively stable molecule at room temperature (see Figure 1). The energy of the *trans-perp* isomer is computed to be 1–3.2 kcal/mol above the *cis-cis* form. The transition state for isomerization between these isomers, the *perp-perp* isomer, has an MP2 energy (including ZPE correction) of 11.4 kcal/mol relative to the *cis-cis* isomer.<sup>37</sup>

HOONO has been studied extensively in the condensed phase, though the most direct spectroscopic studies come from matrix-isolation work. Lee and colleagues<sup>47–50</sup> reported vibrational and UV absorption spectra of HOONO trapped in rare gas matrixes. The observed infrared bands matched frequencies and intensities predicted by ab initio calculations for the *cis-cis* and *trans-perp* isomers. The *cis-perp* isomer is predicted to have vibrational frequencies similar to those of the *trans-perp* isomer, but it was ruled out on the basis of intensity patterns.

In the gas phase, two earlier attempts at infrared absorption spectroscopy failed to detect HOONO. Burkholder et al.<sup>51</sup> attempted to prepare HOONO in a fast-flow multipass cell using a variety of methods ranging from microwave discharge to direct synthesis with  $\text{H}_2\text{O}_2$  and  $\text{NOBF}_4$ . They estimated an upper limit for HOONO yield of 5% based on sensitivity arguments, and an  $\text{HONO}_2$  yield of 75% + 25%–10% from mass balance. More recently, Dransfield et al.<sup>52</sup> attempted to detect HOONO formed by reaction 1 with reaction modulation FTIR spectroscopy, but found no unidentified bands that could be assigned to HOONO in the range 700–3200  $\text{cm}^{-1}$ . They estimated an upper limit for HOONO of 3–4% based on mass balance arguments.

Direct evidence for formation of HOONO in the gas phase by reaction 2 has been reported only recently. In 2001, Donahue et al.<sup>53</sup> described a series of  $^{18}\text{O}$  isotopic scrambling experiments that supported the existence of reaction 2 and led to an estimate of the low-pressure branching ratio of  $k_2^\circ/k_1^\circ = 0.17$  at room temperature. Nizkorodov and Wennberg<sup>54</sup> then reported

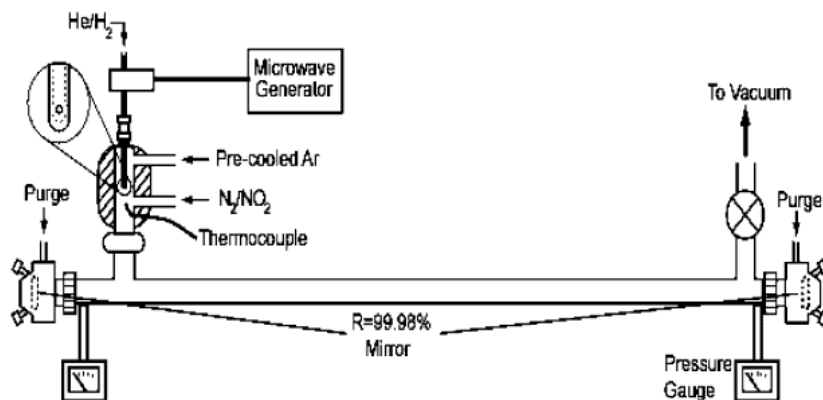


**Figure 2.** Overview of the experimental apparatus. A microwave discharge is used to produce H atoms that are introduced into an Ar flow through the injector tip (exploded view), which then mixes with an  $\text{NO}_2/\text{N}_2$  flow. The H atoms react by  $\text{H} + \text{NO}_2 \rightarrow \text{OH} + \text{NO}$  to form OH radicals. The OH radicals react with  $\text{NO}_2$  to form HOONO and HONO<sub>2</sub> within 1 cm. Infrared absorption spectra of products are detected downstream in the ringdown cavity, formed by two high-reflectivity mirrors (dashed lines,  $R = 99.98\%$  at  $2.8 \mu\text{m}$ ).

the first spectroscopic observation of gas-phase HOONO from the reaction of OH and  $\text{NO}_2$ . They observed the  $2\nu_1$  overtone spectrum of HOONO formed in a low-pressure discharge flow cell using action spectroscopy, detecting OH by LIF after predissociation of the overtone-excited molecules. They observed several bands which they tentatively assigned to the isomers of HOONO and combination bands. They estimated that the HOONO yield was  $5 \pm 3\%$  at 253 K and 20 Torr. In 2002, Hippler et al.<sup>32</sup> reported kinetic evidence for channel 2. They observed a biexponential decay in the OH LIF signal in the reaction  $\text{OH} + \text{NO}_2$  at 5–100 bar and 430–475 K, which they modeled as rapid loss of OH by reactions 1 and 2, followed by slower decomposition of HOONO by the reverse rate  $k_{-2}$ . They found the enthalpy of reaction 2 at this temperature range to be  $\Delta H_2^{\circ}(0) = -19.8 \text{ kcal/mol}$ , in good agreement with the theoretical predictions of the *cis-cis* HOONO dissociation energy  $D_0$ .

In principle, the branching ratio between reactions 1 and 2 can be measured by infrared absorption spectroscopy of both HOONO and HONO<sub>2</sub>, but the difficulty of detecting HOONO at such low concentrations ( $< 10^{12} \text{ cm}^{-3}$ ) has been compounded by possible spectral interference from the high concentrations of HONO<sub>2</sub> and  $\text{NO}_2$ . However, the lowest energy isomer, *cis-cis* HOONO, can be distinguished from HONO<sub>2</sub> in the  $3 \mu\text{m}$  region, because the OH stretch is significantly red-shifted relative to that of HONO<sub>2</sub>. Ab initio calculations indicate that this shift arises from a hydrogen-bonding interaction between the H atom and the terminal O atom which occurs only in the *cis-cis* conformation (see Figure 1).<sup>36,37</sup> Lo and Lee observed this band at  $3285 \text{ cm}^{-1}$  in Ar matrix.<sup>55</sup> In contrast, they observed the  $\nu_1$  band of the *trans-perp* isomer at  $3563.4$  and  $3545.7 \text{ cm}^{-1}$  (different substitution locations), nearly coincident with the OH stretch of nitric acid at  $3550.0 \text{ cm}^{-1}$ .

In this work, we report a joint experimental/theoretical study to measure the *cis-cis* HOONO-to-HONO<sub>2</sub> branching ratio from the reaction  $\text{OH} + \text{NO}_2 + \text{M}$ , which we denote  $k_2(c-c)/k_1$ , in a low-pressure discharge flow reactor. We have exploited the high sensitivity of infrared cavity ringdown spectroscopy (IR-CRDS) to observe directly the absorption spectra of *cis-cis* HOONO as well as HONO<sub>2</sub> in the  $3 \mu\text{m}$  region. The branching ratio can be determined from the integrated intensities of the OH stretch modes of both species with the aid of ab initio vibrational band strengths calculated at the QCISD and CCSD-(T)/cc-pVTZ level. Finally, we perform statistical calculations

to predict the rate that the *trans-perp* HOONO isomer converts to the *cis-cis* form and compute the *trans-perp* HOONO energy. From these results, we infer that the observed *cis-cis* yield most likely represents the total HOONO yield.

## Experiment

An overview of the experimental apparatus is shown in Figure 2. The flow cell comprised two regions, a discharge flow reactor in which the  $\text{OH} + \text{NO}_2$  reaction took place, and a long path spectroscopic detection region. In the reaction region, hydrogen atoms were formed by microwave discharge and thermalized by injection into a flow of pre-cooled argon. This gas was then mixed with  $\text{NO}_2$  seeded in  $\text{N}_2$  to produce OH radicals by the reaction



with  $\text{NO}_2$  in excess. The OH products of reaction 3 then reacted with the  $\text{NO}_2$ . The resulting mixture of products flowed into the detection region, where they were detected by infrared absorption from  $2.6$  to  $3.4 \mu\text{m}$  using cavity ringdown spectroscopy. Experiments were performed over the pressure range 5 to 40 Torr and the temperature range 240 to 360 K.

The cell was constructed of Pyrex and quartz, and the interior walls were coated with halocarbon wax to minimize wall reactions. The entire system was evacuated by a 52-cfm mechanical pump through a stopcock and an  $\text{LN}_2$ -trapped foreline. Two capacitance pressure transducers were located at either end of the detection region to verify constant pressure throughout the cell during measurements. All of the gases used in these experiments were UHP grade (99.999%) or higher purity. Six mass flow transducers coupled with needle valves enabled us to vary the flows of the reactant gases as well as the purge flows over the ringdown mirrors. The flows and estimated concentrations of reactants are listed in Table 1. The linear flow velocity was typically 100–200 cm/s, and the total residence time in the cell was typically 200 ms.

**A. OH +  $\text{NO}_2$  Reaction Region.** H-atoms were produced in a microwave discharge source.  $\text{H}_2$  was mixed in a 1:200 ratio with He that had been passed through a  $\text{LN}_2$ -cooled zeolite trap to remove condensable impurities. The mixture then flowed through a quartz capillary (4-mm i.d.) in which a discharge was maintained by an Evenson microwave cavity. The capillary extended collinearly into the main reactor cell (2.5-cm i.d.) in

**TABLE 1: Typical Flows and Concentrations for Branching Ratio Measurements**

species	flow/sccm	concentration/ cm <sup>-3</sup> (300 K, 20 Torr)
He	615	$2.85 \times 10^{17}$
Ar	515	$2.38 \times 10^{17}$
N <sub>2</sub>	242	$1.12 \times 10^{17}$
NO <sub>2</sub>	13	$6.0 \times 10^{15}$
H <sub>2</sub>	3	$1.38 \times 10^{15}$

which pre-cooled Ar gas flowed. The discharge gas was injected in jets perpendicular to the Ar flow through small holes near the capillary tip. Turbulent mixing of the discharge gas with the Ar flow ensured an even distribution of H atoms in the reactor and helped to dissipate heat from the discharge.

A mixture of 4% NO<sub>2</sub> in N<sub>2</sub> by volume (Matheson, certified gravimetrically) was introduced through a 4-mm i.d. inlet approximately 1 cm downstream from the end of the quartz discharge tube. We adjusted the location of the H-atom injection with respect to the N<sub>2</sub>/NO<sub>2</sub> entrance to allow for the mixing and cooling of the discharge flow, while keeping wall loss of H-atoms to a minimum. At the concentrations used in this experiment, the reaction of H and NO<sub>2</sub> was essentially complete within microseconds, while the subsequent association reaction of OH + NO<sub>2</sub> + M was complete in <500 μs. Thus, products from reactions 1 and 2 were formed within a few millimeters along the flow, well before the gas entered the spectroscopy region. Although H + NO<sub>2</sub> is known to produce high yields of vibrationally excited OH,<sup>56</sup> NO<sub>2</sub> is an effective quencher. Furthermore, OH(*v*) + NO<sub>2</sub> will produce highly excited transient adducts which will not stabilize to form products.

The temperature of the reaction region was measured with a calibrated type “T” thermocouple placed in the center of the reaction zone. The temperature at the point of reaction was slightly higher than the reactor walls, because the He/H<sub>2</sub>/Ar mixture had not fully equilibrated. Thermal gradients led to temperature variations of up to ±3° C across the reaction region; these uncertainties are reflected in abscissa error bars in the temperature dependence.

**B. Detection of HOONO and HONO<sub>2</sub>.** Infrared absorption spectra of the reaction products were obtained in a long-path cell situated downstream of the reaction region, 8 cm from the NO<sub>2</sub> injection point. Most spectra were recorded in a room-temperature cell (1.9-cm i.d.) which had a cavity length  $L = 81.5$  cm and a sample absorption path length  $L_s = 51$  cm through the reactant gas mixture. The absorption path length  $L_s$  was determined by the distance from the gas inlet port to the pump-out port. We occasionally used a second jacketed cell ( $L = 67$  cm,  $L_s = 32$  cm, 2.5-cm i.d., 20 cm distance from the NO<sub>2</sub> inlet port), which allowed us to vary the detection cell temperature in order to investigate temperature-dependent wall loss and residence time effects.

Absorption spectra of the reaction products were recorded by pulsed cavity ringdown spectroscopy.<sup>57–59</sup> A mid-infrared laser pulse was injected into an optical cavity made by two high-reflectivity infrared mirrors ( $R = 99.98\%$ , centered at  $\lambda = 2.8$  μm, 6 m radius of curvature) sealed to the ends of the detection cell. Each mirror was separated from the main flow of gas by a purge volume approximately 15 cm long. Dry argon flowed over the mirrors (8 sccm over each mirror) and through the purge volumes to protect the mirrors and to minimize losses in reflectivity due to deposition.

We produced tunable (2.6–3.4 μm) mid-IR in a two-stage, optical parametric amplifier (OPA)<sup>60</sup> by mixing the second harmonic of an Nd:YAG laser and the output of a tunable dye

laser in a pair of KTP crystals.<sup>60</sup> The OPA produced an IR beam with energy  $E \approx 1$  mJ/pulse and diameter  $d \approx 2$  mm after transmission through three filters to remove the residual 532 and 630 nm light. The IR line width was  $\Gamma \approx 1$  cm<sup>-1</sup>. The IR wavelength was typically calibrated using the frequencies of known HONO and HNO<sub>3</sub> peaks in the spectrum. The IR beam was aligned into the cavity, and the residual beam exiting the cell was focused tightly onto a 1-mm diameter InSb detector (Infrared Associates). Each ringdown trace was amplified and then accumulated with a 300 MHz bandwidth digital oscilloscope with 8-bit digitizer/12-bit averager (Tektronix TDS 320). For each point in a spectrum, typically 32 ringdown traces were averaged by the oscilloscope before transfer to the PC, which then fit the data to a single-exponential function and constant baseline by the Levenberg–Marquardt algorithm.<sup>61</sup>

The ringdown lifetime of radiation trapped in an evacuated optical cavity of length  $L$  with mirrors of reflectivity  $R$  is  $\tau_0 = L/c(1 - R)$ , where  $c$  is the speed of light.<sup>62–64</sup> Typical empty-cell ring-down times were  $\tau_0 \approx 10$  μs, in good agreement with the stated mirror reflectivity (99.98% at the peak wavelength). In the presence of an absorber, the lifetime is given by  $\tau = L/c(1 - R + \alpha L_s)$ , where  $\alpha = [X]\sigma_X$ ,  $\sigma_X$  is the extinction coefficient of the absorber X, and  $L_s$  is the absorption path length through the sample. The measured extinction coefficient is then

$$\alpha = \frac{L}{cL_s} \left( \frac{1}{\tau} - \frac{1}{\tau_0} \right)$$

The possible dependence of the measured extinction coefficient on the concentration of absorber will be discussed in detail below.

Spectra of reaction products were typically recorded by scanning the spectral region of interest with the discharge on and off, and subtracting the two scans. This subtraction eliminated background due to species present in the absence of reaction, as well as to the wavelength-dependent ringdown loss of the mirrors.

We estimated the sensitivity of our CRDS setup from  $\Delta\tau$ , the minimum detectable change in  $\tau$ .<sup>63</sup> In a typical run, we found  $\Delta\tau/\tau_0 \approx 2\%$  (averaging 32 laser shots), giving a minimum detectable absorption of  $\alpha_{\min} \approx 1 \times 10^{-7}$  cm<sup>-1</sup> ( $1.8 \times 10^{-7}$  cm<sup>-1</sup> √Hz) for mirrors with reflectivity  $R = 99.97\%$ . For the detection of HONO<sub>2</sub> with the  $\nu_1$  band, which has an integrated intensity of  $9.5 \times 10^{-18}$  cm<sup>2</sup>/molecule,<sup>65</sup> the minimum detectable concentration of nitric acid was  $[\text{HONO}_2]_{\min} \approx 5 \times 10^{11}$  molecules/cm<sup>3</sup> at a single point in the R-branch. Integration over the OH stretching band further improved the sensitivity by roughly  $N^{1/2}$ , where  $N \approx 20$  is the number of data points making up fwhm of the band.

We investigated the effect of the purge gas flow rate on the detection of products. The linear flow velocity of Ar through each of the purged volumes was  $\approx 3$  cm/s, or 0.6% of the total flow. We measured both product absorption signals while independently varying the purge flow at the inlet and outlet ends of the detection cell from 0.5% to 9%. There was a gradual decrease (approximately 20%) in the absorption by both HONO<sub>2</sub> and HOONO as we increased the purge flow rates to 9%, but the fractional yield of HOONO remained constant. Thus, while some reaction gas mixture entered the purged volume at the flow rates used in this experiment, these gases were flushed out quickly and did not affect branching ratio measurements.

### Computational Methodology

**A. Ab Initio Calculations of Structure, Energetics, and Intensities.** Ab initio electronic structure calculations were

TABLE 2: Computed Molecular Constants for the *cis-cis* and *trans-perp* Conformational Isomers of HOONO

	cis-cis				trans-perp		
	QCISD cc-pVTZ <sup>a</sup>	QCISD(T) cc-pVTZ <sup>a</sup>	CCSD(T) cc-pVTZ	MP2 6-31G(d) <sup>b</sup>	QCISD cc-pVTZ	CCSD(T) cc-pVTZ	MP2 6-31G(d) <sup>b</sup>
$\Delta E_0$ (kcal/mol)						3.4	2.9 <sup>c</sup>
$A$ (MHz)	21726	21262	21310	20900	55716	54127	52576
$B$	8133	8041	8081	7949	5060	4977	4902
$C$	5917	5835	5859	5759	4709	4627	4550
$\nu_1$ (cm <sup>-1</sup> )		3496( <i>a</i> )	3521	3547 <sup>d</sup>		3780	3841 <sup>e</sup>
$\nu_2$		1649( <i>a</i> )	1630	1595		1736	1720
$\nu_3$		1461( <i>a</i> )	1458	1476		1412	1408
$\nu_4$		939( <i>a</i> )	969	991		992	999
$\nu_5$		796( <i>a</i> )	838	858		816	811
$\nu_6$		618( <i>a</i> )	723	776		497	443
$\nu_7$		397( <i>a</i> )	419	418		366	373
$\nu_8$		515( <i>a</i> '')	523	532		302	311
$\nu_9$		363( <i>a</i> '')	383	360		211	219

<sup>a</sup> Refs 43,44. <sup>b</sup> McGrath and Rowland, ref 37. <sup>c</sup> MP2/6-311+G(3df,2p), ref 37. <sup>d</sup> Frequencies calculated with the 6-311G(2df,2p) basis set. <sup>e</sup> Frequencies calculated with the 6-311G(d,p) basis set.

performed to predict (a) structures, vibrational frequencies, and energies of the *cis-cis* and *trans-perp* isomers of HOONO, and (b) band intensities of HOONO, HO<sub>2</sub>NO<sub>2</sub>, and HONO<sub>2</sub>. Calculations were performed with the Gaussian 98<sup>66</sup> and MOLPRO<sup>67</sup> programs. Coupled cluster theory<sup>68</sup> with single and double excitations, with perturbative estimates of connected triples CCSD(T), was used along with the quadratic configuration interaction method (QCISD(T) and QCISD).<sup>69</sup> The QCISD(T) method is correct through fourth-order terms, and it includes the same fifth-order terms as the CCSD(T) method. In the absence of large multireference effects or large single excitation amplitudes, the QCISD(T) method should be very reliable,<sup>69</sup> and its performance is very similar to that of CCSD(T).<sup>70</sup> The calculations were performed with the Dunning correlation-consistent polarized valence basis sets. The two basis sets used throughout this study are the cc-pVDZ basis set (3s2p1d for C, N, and O; 2s1p for H) and then the cc-pVTZ basis set (4s3p2d1f for C, N, and O; 3s2p1d for H).<sup>71,72</sup> From many benchmark calculations with extended basis sets, the CCSD(T) and QCISD(T) methods have shown that high accuracy can be achieved for the molecular structure and vibrational frequencies.<sup>73,74</sup> Vibrational frequencies were calculated with both the QCISD and CCSD(T) methods. Intensities were calculated with the QCISD method and scaled to estimate the CCSD(T) intensities by the factor 0.968. The scale factor was determined from a calibration set of molecules of well-known intensities and also from calculation of intensities for the calibration set of molecules using the CCSD(T) method. The CCSD(T) intensities were calculated with MOLPRO. The calibration set was HCN, H<sub>2</sub>O, CH<sub>4</sub>, and CH<sub>3</sub>O. A total of 14 intensities were used in the scale factor determination.

**B. Transition Dipole Moment Vector.** Additional calculations were carried out to determine the orientation of the vibrational transition dipole moment for the  $\nu_1$  band of HOONO. The electrostatic dipole moment was computed at the B3LYP/cc-pVTZ level using Gaussian 98 for several displacements from equilibrium along the  $Q_1$  normal coordinate using the  $L$  matrix given at the equilibrium geometry. The resulting dipole vector functions were fit to a polynomial and then numerically integrated over harmonic oscillator wave functions to obtain the three components of the transition dipole matrix element in the principal axis frame.

**C. Calculations of Isomerization Rates.** We computed the formation and isomerization rates of the isomers of HOONO using the program MultiWell.<sup>75,76</sup> We focused in particular on the rate of isomerization from the *trans-perp* isomer to the lower

energy *cis-cis* isomer. For the current calculation, we used parameters for the *perp-perp* transition state for rotation of the OONO dihedral angle, which lies between the *trans-perp* and *cis-perp* isomers. The energy of the *perp-perp* isomer was computed at the MP2/6-311G(3df,2p) level with MP2/6-31G(d) frequencies by McGrath and Rowland (note that the MP2 energies listed in their Table 2 are not corrected for zero-point energy).<sup>37</sup> We employed the *trans-perp* and *cis-cis* vibrational frequencies from the same calculation, but we used our CCSD(T) calculation of the *trans-perp* energy. We also performed some calculations of the initial branching ratios for reactions 1 and 2, using transition state parameters based on those of Golden and Smith.<sup>31</sup> Energy transfer collisions were described by the single-exponential model<sup>75</sup> with  $\alpha = 45 \text{ cm}^{-1} + 0.005 E_{\text{upper}}(\text{cm}^{-1})$ , and Lennard-Jones parameters  $\epsilon = 180 \text{ K}$  and  $\sigma = 4.2 \text{ \AA}^2$ .

## Results

**A. Spectroscopy of OH + NO<sub>2</sub> Products.** Figure 3 shows a room-temperature scan from 3200 to 3700 cm<sup>-1</sup> taken in 0.2 cm<sup>-1</sup> steps with the flow cell conditions shown in Table 1. The full-scale spectrum, shown in the inset, is dominated by the  $\nu_1$  HONO<sub>2</sub> transition. With the discharge off, the HONO<sub>2</sub> spectrum was approximately 8–10 times weaker. This small background HONO<sub>2</sub> signal, which was always present in the cell during the experiments, arose largely from slow desorption from passivated walls. Several other absorption bands were evident in this region. All of the bands had partially resolved rotational structure. The smaller bands could be assigned to known transitions: the  $2\nu_2$  band of HONO<sub>2</sub>, the  $2\nu_2$  and  $\nu_1$  bands of both *cis*-HONO and *trans*-HONO, and the  $2\nu_3$  transition of NO<sub>2</sub>. There remained one unidentified band centered at 3306 cm<sup>-1</sup>.

**B. Assignment of the *cis-cis* HOONO Band.** Figure 4 shows the spectrum from 3250 to 3375 cm<sup>-1</sup> after subtraction of the empty-cell background. The sharp features at 3260 and 3372 cm<sup>-1</sup> were assigned to the Q-branches of the  $2\nu_2$  transitions of *cis*- and *trans*-HONO, respectively. A clearly defined set of P, Q, and R subbands centered at 3306 cm<sup>-1</sup> was identifiable between these features. We assigned this band to the  $\nu_1 = 0 \rightarrow 1$  (O–H stretch) transition of *cis-cis* HOONO for the following reasons.

(1) Chemistry. This band was not observed if the discharge was off, even with all reagent gases (Table 1) present. We did not observe any absorption in this region when we recorded experimental reference spectra of either HONO or HONO<sub>2</sub>

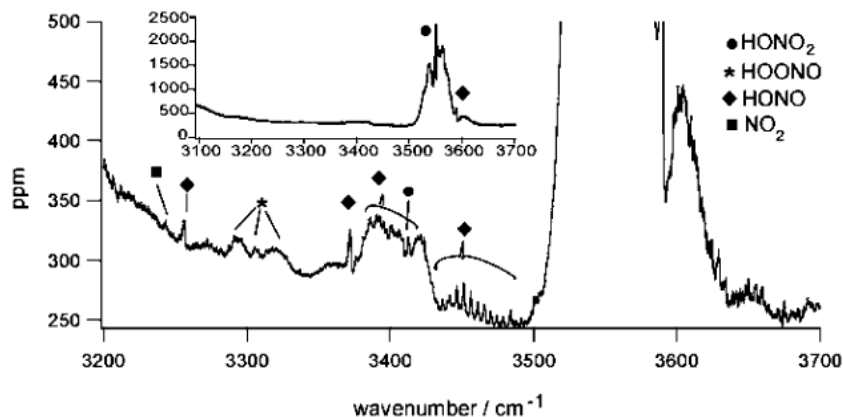


**Figure 3.** Absorption spectrum of the products of OH + NO<sub>2</sub> at 20 Torr and 300 K recorded by infrared cavity ringdown spectroscopy. No background has been subtracted; the varying baseline is due to the underlying variations in ringdown mirror reflectivity. The laser line width is 1 cm<sup>-1</sup> and the step size of the scan is 0.2 cm<sup>-1</sup>. The full scale spectrum, shown in the inset, shows that nitric acid is the dominant product in the reaction OH + NO<sub>2</sub>. Weaker bands in the magnified scan assigned to known transitions are marked: HONO<sub>2</sub> (●), HONO (◆), or NO<sub>2</sub> (■). The only unassigned band, at 3306 cm<sup>-1</sup>, is attributed to the  $\nu_1$  transition of *cis-cis* HOONO (\*).

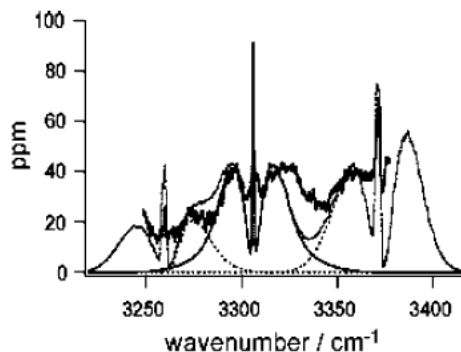


**Figure 4.** Spectrum of the *cis-cis* HOONO  $\nu_1$  band and adjacent  $2\nu_2$  bands of *cis* and *trans*-HONO, with the ringdown baseline subtracted. The thick line is the experimental data, and the gray line is the sum of three simulated spectra: *cis-cis* HOONO (thin line, centered at 3306 cm<sup>-1</sup>), *cis*-HONO (short dash, 3260 cm<sup>-1</sup>), and *trans*-HONO (long dash, 3372 cm<sup>-1</sup>).

generated from bubbled samples. Furthermore, the band was not present if either NO<sub>2</sub> or H<sub>2</sub> was removed with the discharge on. We found no detectable spectra of H<sub>2</sub>O<sub>2</sub> or HO<sub>2</sub>, which have band origins closer to 3400 cm<sup>-1</sup>, or of HO<sub>2</sub>NO<sub>2</sub>, which has an absorption at 3540 cm<sup>-1</sup>. Thus, this band arose from a reaction product but could not be attributed to any of the primary reactant or product species (HONO, NO, NO<sub>2</sub>, HONO<sub>2</sub>) or other conceivable products (H<sub>2</sub>O<sub>2</sub>, HO<sub>2</sub>NO<sub>2</sub>).

(2) Deuterium Substitution. When D<sub>2</sub> was substituted for H<sub>2</sub> in the discharge flow, the band at 3306 cm<sup>-1</sup> disappeared but the two adjacent DONO  $2\nu_2$  (NO<sub>2</sub> stretch overtone bands) were still readily observable. These results indicate that this mode most likely involved a hydride X–H stretch.

(3) Band Position and Intensity. The frequency of the band origin, 3306 cm<sup>-1</sup>, red-shifted relative to the OH stretch of HONO<sub>2</sub> by 245 cm<sup>-1</sup>, was in good agreement with the position expected for the *cis-cis* isomer of HOONO from both experiment and theory. The observed band center was close to the 3285 cm<sup>-1</sup> origin of the  $\nu_1$  fundamental of *cis-cis* HOONO observed in matrix isolation experiments; the difference can be accounted for by matrix-induced shifts. It also matched the fundamental position estimated by Nizkorodov and Wennberg.<sup>54</sup>

based on their preliminary assignment of a band at 6365 cm<sup>-1</sup> to the  $\nu_1 = 0 \rightarrow 2$  overtone transition of *cis-cis* HOONO. Their overtone assignment, taken in conjunction with our observation of the fundamental band, would give  $\omega_e = 3430$  cm<sup>-1</sup> and  $\omega_e x_e = 62$  cm<sup>-1</sup> for the  $\nu_1$  band of HOONO. This harmonic frequency lies close to  $\omega_e = 3521$  cm<sup>-1</sup>, predicted by our CCSD(T)/cc-pVTZ calculations for the *cis-cis* isomer of HOONO. The observed frequency did not match the OH stretch frequencies of the other stable isomer(s) (or of the predicted saddlepoints) of HOONO, all of which have frequencies close to that of nitric acid ( $\omega_{\text{exp}} = 3550$  cm<sup>-1</sup>).

Finally, the integrated band intensity was approximately 3% of the integrated intensity of the  $\nu_1$  band of HNO<sub>3</sub>. This was consistent with expectations of a relatively low HOONO yield, assuming the two bands had similar absorption cross sections. A quantitative assessment of the HOONO yield is given below.

**C. Ab Initio Calculations.** There have been a number of ab initio calculations on the isomers of HOONO. Here we performed QCISD, QCISD(T), and CCSD(T)/cc-pVTZ calculations on *cis-cis* and *trans-perp* conformers of HOONO, to have a consistent set of high-level spectroscopic constants for the two bound isomers. A third isomer, the *cis-perp* conformation, was not found to be stable. Computational results on the torsional potentials will be reported elsewhere.<sup>46</sup>

Table 2 lists results for the rotational constants and vibrational frequencies of the two isomers, along with a comparison with the MP2 calculations of McGrath and Rowland.<sup>37</sup> The numbering of the normal modes of the *trans-perp* isomer are ordered in descending frequency, while the modes of the *cis-cis* isomer, which has C<sub>s</sub> symmetry, are based first on the symmetry *a'* and then *a''*. In general, the frequencies and rotational constants are close to the MP2 results.

In addition, we report the CCSD(T)/cc-pVTZ energy of the *trans-perp* isomer relative to the lowest energy *cis-cis* geometry to be  $\Delta E_0 = +3.4$  kcal/mol, including zero-point correction. The dissociation energy of the *cis-cis* isomer has been reported at a higher level of theory; the best estimate is 18.3 kcal/mol.<sup>44</sup>

To determine the relative yields of HOONO and HONO<sub>2</sub>, we needed the relative absorption cross sections of the respective fundamental  $\nu_1$  transitions. The band strength of nitric acid has been measured, but not that of HOONO. We therefore relied on ab initio intensities computed at equivalent levels of theory

**TABLE 3: Calculated Integrated Intensities for  $\nu_1$  (O–H Stretch) Vibrational Transitions in  $\text{km mol}^{-1}$ , and Comparison with Previous Experimental Values**

	HONO <sub>2</sub>	cis-cis HOONO	trans-perp HOONO	HOONO <sub>2</sub>
QCISD/cc-pVTZ <sup>a</sup>	98.6	34.3	50.1	52.8
CCSD(T)/cc-pVTZ	95.4	33.2	48.6	51.2
experiment		57.0 ± 2.8 <sup>b</sup>		36.2 ± 4.4 <sup>c</sup>

<sup>a</sup> Scaled by 0.968 to estimate CCSD(T) intensities (see text). <sup>b</sup> Ref 65. <sup>c</sup> Ref 87.

to determine the ratio of the absorption strengths of *cis-cis* HOONO and HONO<sub>2</sub>. To estimate the error that may be associated with such a calculation, we also computed the intensity for pernitric acid, HO<sub>2</sub>NO<sub>2</sub>, a molecule of similar composition which, like HOONO, possesses an OH stretch coupled to a peroxide bond.

Table 3 shows the integrated intensities for the OH stretches in HOONO, HONO<sub>2</sub>, and HO<sub>2</sub>NO<sub>2</sub> computed with the QCISD(T)/cc-pVTZ and CCSD(T)/cc-pVTZ methods, as well as a comparison to published values. The QCISD(T) calculations were scaled to estimate the CCSD(T) intensities. While the calculated intensities of HONO<sub>2</sub> and HO<sub>2</sub>NO<sub>2</sub> are greater than the experimental values by 67% and 41%, respectively, the computed HONO<sub>2</sub>-to-HO<sub>2</sub>NO<sub>2</sub> intensity ratios are 1.86 at the CCSD(T) level of theory, while the experimental ratio is 1.57. Thus, the computed ratios—though not the absolute magnitudes—agree with experiment to within 18%.

The CCSD(T) calculations gave an intensity ratio of 2.87 for HONO<sub>2</sub> to *cis-cis* HOONO, and 1.96 for HONO<sub>2</sub> to *trans-perp* HOONO; the scaled QCISD(T) ratios were nearly identical. The integrated absorbance of HOONO must be corrected by this ratio to determine the relative HOONO-to-HONO<sub>2</sub> product concentrations. The comparison with pernitric acid suggests that this value should be accurate to within roughly 20%. This estimation of the error is based on a single calibration point; hence, we cannot estimate the statistical uncertainty, but IR absorbances calculated at this level of theory, even within the double harmonic oscillator approximation, are typically accurate to within 20%.<sup>77,78</sup> By estimating the ratio of intensities of similar stretch modes (OH stretches), systematic errors such as anharmonicity are at least partially corrected, though the *cis-cis* HOONO has an apparent hydrogen-bonding interaction not present in either HONO<sub>2</sub> or HO<sub>2</sub>NO<sub>2</sub>.

Lower-level B3LYP calculations were performed to predict the orientation of the vibrational transition dipole moment for the  $\nu_1 = 0 \rightarrow 1$  transition of *cis-cis* HOONO. The transition dipole moment vector computed as described above was  $(\mu_a, \mu_b, \mu_c) = (0.041 \text{ D}, 0.064 \text{ D}, 0.0 \text{ D})$ . This vector differs slightly from the direction of the OH bond. This calculation then predicts a hybrid band with a 2.3:1 ratio in *b*-type to *a*-type character.

**D. Modeling the HOONO  $\nu_1$  Band.** With these *ab initio* predictions, we modeled the expected rotational contours of the  $\nu_1$  band of *cis-cis* HOONO using the asymmetric rotor program ASYROT.<sup>79</sup> We made the rigid rotor approximation and used the same set of rotational constants for the *cis-cis* isomer (from the *ab initio* calculations) for both the upper and lower states, because we had no information on the change in geometry upon excitation of the  $\nu_1 = 0 \rightarrow 1$  transition.

To compare the simulation with the 3306  $\text{cm}^{-1}$  spectrum, we first had to subtract the contributions to the observed spectrum from the adjacent  $2\nu_2$  bands of *cis*-HONO and *trans*-HONO, whose wings overlapped with the HOONO band. We modeled the rotational contours of the HONO bands,<sup>79</sup> using asymmetric rotor constants from high-resolution FTIR data.<sup>80,81</sup>

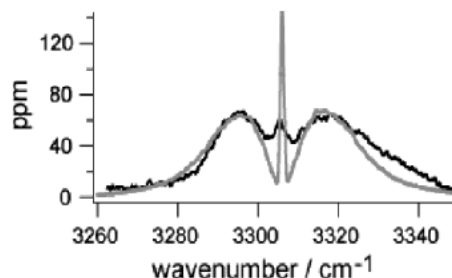


**Figure 5.** Comparison of the experimental *cis-cis* HOONO  $\nu_1$  spectrum (with background and HONO  $2\nu_2$  overtone bands subtracted) and a simulation (grey line) computed as a hybrid band with ratio  $I_b/I_a = 2.3$  using *ab initio* rotational constants.

The modeled spectra matched reference spectra of HONO taken with this apparatus reasonably well. Figure 4 shows the fit of the modeled *cis*- and *trans*-HONO spectra.

In Figure 5, a scan of HOONO from 3245 to 3380  $\text{cm}^{-1}$  taken at 0.2  $\text{cm}^{-1}$  steps with the background and HONO contributions subtracted, is compared with the simulation based on the *ab initio* predictions and a  $I_b/I_a$  ratio of 2.3. The simulation is in good agreement with the observed spectrum. We varied the orientation of the transition dipole moment, but found that the spectrum could best be fit as a hybrid band of *a*-type and *b*-type transitions. A range of  $I_b/I_a$  values from 1 to 4 was acceptable, because the Q branch blended with the P and R branches, making it difficult to estimate the relative area of the Q branch. This range is consistent with the predicted ratio  $I_b/I_a = 2.3:1$ .

The observed HOONO spectrum has a broader Q branch which partially blends with the P and R branches and a broader R branch shaded to the blue. We attribute these discrepancies to (a) the use of identical upper and lower rotational constants, and (b) contributions from sequence bands, progressions, or hot bands of the low-frequency modes of the loosely bound ring structure. The Q branch, in particular, is not expected to be as sharp as predicted by the simple rigid-rotor approximation, but the relative intensity roughly does match the observed spectrum. Blue-shading of the spectrum may arise from intramolecular hydrogen bond tightening in the vibrationally excited state, leading to a more compact geometry and slightly larger upper state rotational constants. Such effects are well documented in hydrogen-bonded complexes. More important, however, will be the significant population in excited low-frequency vibrations. Our CCSD(T)/cc-pVTZ calculations predict three low-frequency modes—the *a''* HOON torsion, the *a''* ONOO torsion, and the *a'* NOO bend—at 383  $\text{cm}^{-1}$ , 523  $\text{cm}^{-1}$ , and 419  $\text{cm}^{-1}$ , respectively. The OH torsion, in particular, will break the hydrogen bond and lead to substantially blue-shifted sequence bands.

Figure 4 shows the total fit of the summed HOONO and HONO contributions. Together, the three spectra account for most of the extinction in this region. If we assume that the remaining area can be attributed to HOONO sequence bands, we estimate the total HOONO integrated signal to be 14% greater than the area of the simulated spectrum alone. This additional area is primarily on the blue side, and is comparable to the expected contribution from torsionally excited modes. The additional absorption is thus most likely to be due to sequence bands.

**E. Lifetime of HOONO.** The detection of *cis-cis* HOONO was performed at room temperature downstream of the reaction region, well after reactions 1 and 2 were complete. Typical total

residence times were 200 ms; thus, any measurements of absorption by HOONO could only be correlated with HOONO concentration if the HOONO lifetime relative to decomposition at room temperature was significantly longer than 200 ms. We varied the residence time from 75 to 250 ms, but we saw no change in the absolute HOONO signal. If the lifetime of HOONO were  $\tau = 200$  ms, we would have expected to see the HOONO signal change by a factor of 1.7 over this time range. Given an uncertainty in HOONO detection of 20%, we estimate that the lifetime must be  $\tau > 500$  ms. Thus, we conclude that the HOONO concentration was not changing appreciably over the time scale of this experiment. These conclusions apply as well to mechanisms which might increase *cis-cis* HOONO population, e.g., isomerization of *trans-perp* HOONO to *cis-cis* HOONO during transit through the detection cell.

**F. Characterization of Wall Losses.** In addition to decomposition of *cis-cis*-HOONO, loss of either HOONO or HONO<sub>2</sub> on the walls of the cell would result in erroneous product yields. While we saw no significant HOONO loss processes at room temperature, we found small decreases in the HOONO and HONO<sub>2</sub> signal at temperatures between 260 and 280 K.

These losses, on the order of 10–20%, increased when a cooled extension was inserted, indicating that some wall deposition or reaction was occurring. At  $T < 250$  K, substantial reversible deposition of HONO<sub>2</sub> occurred. Our results are in qualitative agreement with unpublished wall loss measurements for HOONO by Fry et al.<sup>82</sup> We therefore limited our HOONO/HONO<sub>2</sub> branching measurements to temperatures above 270 K.

**G. Integrated Absorbances of HOONO and HONO<sub>2</sub>.** Integrated absorbances of the  $\nu_1$  bands of both HOONO and HONO<sub>2</sub> were obtained by scanning the respective  $\nu_1$  bands several times, recording discharge-on and discharge-off spectra, taking the difference, and then summing the runs. The bands were then numerically integrated.

We typically scanned each HOONO spectrum over the range 3250 to 3375  $\text{cm}^{-1}$  and fit the observed bands to a composite spectrum from the simulated *cis*-HONO *trans*-HONO, and *cis-cis* HOONO spectra, allowing contributions from each of the three molecules to vary independently. We then used the area under the HOONO curve, scaled to account for the total area of the observed HOONO spectrum in Figure 5, to obtain the integrated HOONO absorption

$$I_{\text{HOONO}} = L_s \int \alpha_{\text{HOONO}}(\nu) d\nu$$

We obtained integrated absorption intensities of nitric acid in a similar manner, scanning from 3490 to 3610  $\text{cm}^{-1}$ . It was essential to subtract the discharge-off spectrum, as there was a significant amount of background HONO<sub>2</sub> accounting for up to 10–15% of the total nitric acid. The spectrum in this region consisted of the main fundamental  $\nu_1$  band of HONO<sub>2</sub>, as well as a sequence band, and a small contribution from the  $\nu_1$  band of *trans*-HONO. To obtain the integrated absorption of HONO<sub>2</sub>, a spectrum of pure bubbled HONO<sub>2</sub> of comparable intensity was fit to our spectra and then integrated. We verified that a combination of the bubbled HONO<sub>2</sub> and *trans*-HONO spectra adequately represented the observed spectral intensity in the region from 3490 to 3610  $\text{cm}^{-1}$ .

The magnitude of the HONO<sub>2</sub> absorption raised concerns about possible systematic errors in the observed absorbance of the nitric acid spectrum. The peak HONO<sub>2</sub> absorption was  $\alpha l \leq 0.002$  (at the Q branch), so that the spectrum did not appear to be saturated in a single pass. However, the HONO<sub>2</sub> spectra

were typically 50 times stronger than the HOONO spectra, and the resulting ringdown lifetime was an order of magnitude greater than the baseline ringdown time.

We therefore performed a series of experiments to examine the ringdown spectra of varying concentrations of HONO<sub>2</sub> from nitric acid mixed with Ar at 20 Torr. We found that the overall absorption band shape varied slightly with HONO<sub>2</sub> concentration. The band shape agreed well with modeled contours at low HONO<sub>2</sub> concentrations, but the P and Q branches appeared to decrease relative to the R branch at higher concentrations. Hence, some apparent nonlinearity in the absorption measurement appeared to be occurring.

The use of a low-resolution laser for cavity ringdown spectroscopy may introduce a potential error. As Zalicki and Zare<sup>63</sup> and Yalin and Zare<sup>83</sup> have shown, when the ratio of the absorption bandwidth to laser bandwidth is  $V < 100$ , the ringdown decay becomes nonexponential. At a given frequency, the laser samples some ensemble of narrow, partially resolved, and unresolved absorption features within the line width of 1  $\text{cm}^{-1}$ . The total signal is the sum of frequency components  $\nu_i$ , each contributing a signal with a decay time  $\tau_i$  determined by the absorption  $\alpha(\nu_i)$ . The resulting ringdown signal in general will not be a single exponential. In a typical experiment, the total signal is then a fit to an effective overall decay, which underestimates the absorption. As the spectrum becomes increasingly congested, however, narrow features blend and the lines can become unresolvable. If the spectral features become much wider than the laser line width, the cavity ringdown spectrum should approach the convoluted low-resolution spectrum. Alternatively, Zalicki and Zare also showed that if the absorbance was weak compared to cavity loss, then the integrated intensity—though not the individual line shape—was correct to within 10%. Furthermore, as Hodges et al.<sup>84</sup> have shown, the spectral profile of YAG-pumped dye lasers is not Gaussian, but composed of fluctuating lines at the cavity mode spacing, which tends to ameliorate the underestimation.

The  $\nu_1$  band of nitric acid is known to have resolvable Doppler-broadened features, but it is highly congested and has not yet been assigned.<sup>85</sup> In the current experiment, the underlying HONO<sub>2</sub> spectrum typically consisted of a set of narrow lines with a Voigt profile from the convoluted Doppler and pressure-broadened line shapes. The ringdown spectra that we recorded possessed partially resolved features.

We therefore determined the deviation of the integrated absorbance measured by CRDS in our branching ratio experiments in a separate experiment, in which we measured the absolute integrated intensity of the  $\nu_1$  band as a function of HONO<sub>2</sub> concentration. N<sub>2</sub> was bubbled through nitric acid and its concentration measured by a 185 nm Hg lamp before dilution with N<sub>2</sub> and passage into the CRDS cell. A detailed description of this experiment, as well as simulations of ringdown spectra based on high-resolution spectra of HONO<sub>2</sub>, will be reported elsewhere.<sup>86</sup> The true integrated intensity was measured at low HONO<sub>2</sub> concentrations, and compared to HONO<sub>2</sub> absorbance measured at the HONO<sub>2</sub> concentrations obtained in the discharge. From these measurements, we concluded that the current branching ratio experiments underestimated the absolute infrared intensity of the  $\nu_1$  band of HONO<sub>2</sub> by 17%.

In contrast, it is likely that the integrated absorbance of the  $\nu_1$  band of *cis-cis* HOONO is correct. First, the HOONO absorption is approximately 10 times less than the mirror loss, thus meeting the criterion of Zalicki and Zare for weak absorption. Second, we expect that this band is highly congested at room temperature. The observed spectrum is relatively

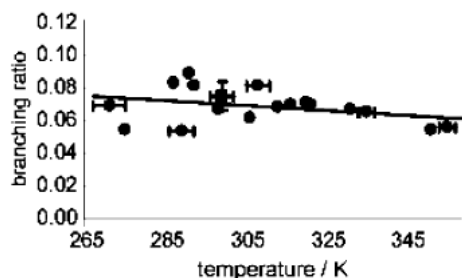


**Figure 6.** Observed ratio of *cis-cis* HOONO to HONO<sub>2</sub> products in the reaction OH + NO<sub>2</sub> as a function of temperature, at 20 Torr (See Table 1 for gas composition). The experimentally measured ratios of the integrated  $\nu_1$  absorption bands were scaled by the computed ratio of absorption cross sections. The abscissa uncertainties are the  $2\sigma$  random errors associated with temperature variations. One point (square) was the mean of measurements on several days.

smooth, with no detectable sub-structure. *cis-cis* HOONO is predicted to be an asymmetric rotor with Ray's parameter  $\kappa = -0.71$ , and the  $\nu_1$  band is predicted to be an  $a-b$  hybrid. Since the OH bond participates in an intramolecular hydrogen-bond, the rotation-vibration interactions cannot be neglected. Finally, several low-frequency modes, including two torsional modes, will have significant populations that will increase the spectral congestion. HOONO has three modes with harmonic frequencies under 500 cm<sup>-1</sup>, whereas the lowest frequency harmonic mode in nitric acid is slightly below 500 cm<sup>-1</sup>. Under these conditions, the "low-resolution" cavity ringdown spectrum of HOONO is more likely to both reproduce the overall shape of the band and yield the correct integrated absorbance.

**H. Determination of the *cis-cis* HOONO/HONO<sub>2</sub> Branching Ratio.** We recorded the integrated absorptions of *cis-cis* HOONO and HONO<sub>2</sub> at a variety of reaction temperatures at 20 Torr, and pressures from 4 to 40 Torr at 300 K. While the temperature of the reaction region was varied, all spectroscopic measurements were performed with the detection cell held at room temperature. Thus, the band contours were independent of reaction conditions, and wall losses in the detection region were negligible. Furthermore, as we demonstrated above, the HOONO lifetimes were sufficiently long that HOONO extinction coefficients were unaffected by the residence time. Thus, the column density in the spectroscopy should accurately reflect the product yield. The HONO<sub>2</sub> integrated absorption was scaled by 1.17 to correct for the error due to cavity ringdown measurement. The HONO<sub>2</sub> concentrations did not vary considerably in the data sets, and we found that use of the same correction factor did not introduce a significant error.

HOONO-to-HONO<sub>2</sub> branching ratios were then obtained by weighting the observed absorption intensity ratios by 2.87, the ratio of the *ab* initio absorption band strengths computed at the CCSD(T)/cc-pVTZ level.

Measurements of the branching ratio were performed at room temperature and 20 Torr on several different days. The variations, most likely arising from source conditions, were  $\pm 0.025$ . Averaging over these results, we determined the 300 K branching ratio to be  $k_2(c-c)/k_1 = 0.075 \pm 0.009$ , where the quoted uncertainty is the  $2\sigma$  standard error of the mean.

Figure 6 shows our measurements of the branching ratio of *cis-cis* HOONO to HONO<sub>2</sub> over the temperature range 270 K to 360 K at 20 Torr total pressure. The *cis-cis* HOONO yield appeared to be almost independent of temperature; the slope of the temperature profile was  $-1.7(\pm 2.4) \times 10^{-4}/\text{K}$  ( $2\sigma$ ). The temperatures plotted were from the thermocouple in the reaction

region. Typical uncertainties in  $T$  due to radial variations of up to  $\pm 3$  K are shown, but the weak temperature dependence leads to little resulting uncertainty in the yield of HOONO.

**I. Uncertainties.** The scatter in the data shown in Figures 6 is due to random errors that include the effects of (a) noise in the collected spectra; (b) uncertainty in the estimation of the integrated band intensities from fitting the band of HOONO, HONO, and HONO<sub>2</sub>; and (c) variations in conditions of the reaction region. As discussed above, there is a temperature uncertainty of up to  $\pm 3$  °C. Our uncertainty in the pressure is 1%. However, the branching ratio depends only weakly on temperature, and thus the error propagated into the branching ratios is negligible.

In addition to the random experimental errors, there are several uncertainties. The largest uncertainty arises from the calculated ratio of absorption cross sections, which we estimate is on the order of 20% on the basis of the difference between the computed and observed ratios of  $\nu_1$  band strengths of HONO<sub>2</sub> and HO<sub>2</sub>NO<sub>2</sub>. A second uncertainty lies in our correction of the integrated HONO<sub>2</sub> absorbance due to the use of the cavity ringdown method. We estimate the error in this correction to be on the order of 10%. Finally, if we conservatively assume that there is resolvable structure in the HOONO spectrum, then the weak absorbance condition of Zalicki and Zare<sup>63</sup> leads to 10% uncertainty in the HOONO intensity. Adding these uncertainties in quadrature to the  $2\sigma$  random error of 0.009(12%), we find that the branching ratio for *cis-cis* HOONO vs HONO<sub>2</sub> products is

$$k_2(c-c)/k_1 = 0.075 \pm 0.020(2\sigma)$$

at room temperature and 20 Torr of the He/Ar/N<sub>2</sub> mixture.

**J. Search for  $\nu_1$  Band of *trans-perp* HOONO.** Our spectroscopic measurements in the 3500–3650 cm<sup>-1</sup> range can also provide a coarse upper bound on the *trans-perp* HOONO concentration. From the matrix isolation studies, the  $\nu_1$  band of *trans-perp* HOONO is near 3550 cm<sup>-1</sup>, under the OH stretch of nitric acid. Our calculations predict that this band is 50% weaker than the  $\nu_1$  band of HONO<sub>2</sub>. This band is likely to be a *c*-type transition, because the OH bond lies nearly perpendicular to the plane of the heavy atoms. Thus, the *trans-perp* OH stretch band should exhibit a sharp Q branch that would be readily observed within the HONO<sub>2</sub> absorption (unless it lies directly under the HONO<sub>2</sub> Q branch). From the absence of any anomalous features or other large discrepancies in the vicinity of the HONO<sub>2</sub> spectrum, we infer that the branching fraction of the *trans-perp* isomer is  $< 20\%$ .

**K. Statistical Calculation of the *trans-perp*  $\rightarrow$  *cis-cis* Isomerization Rate.** We simulated the isomerization process, assuming that these isomers are separated by the transition state with geometry corresponding to the *perp-perp* saddle point computed at the MP2/6-311G(3df,2p) level by McGrath and Rowland.<sup>37</sup> This transition state has an energy of 11.4 kcal/mol relative to the *cis-cis* isomer at the MP2 level, including zero-point energy. For consistency in the density of states calculations, we used their MP2 vibrational frequencies and geometries for all three conformers, *cis-cis*, *trans-perp*, and *perp-perp*, but used our best CCSD(T) estimate for the *trans-perp* energy relative to the energy of *cis-cis* HOONO.

We found that the nascent HOONO molecules establish a rapid ( $k > 10^{10}$  s<sup>-1</sup>) microcanonical equilibrium between the two isomers as they are slowly ( $k_{\text{collision}} \approx 10^8$  s<sup>-1</sup> at 13 Torr) driven down the internal energy ladder by collisions. Because of its smaller moments of inertia (centrifugal barrier effect) and larger degree of "floppiness", the *trans-perp* isomer has a density

of states comparable to that of the *cis-cis* isomer at energies above the isomerization barrier. Thus, a large fraction of excited HOONO molecules ( $\approx 30\%$ ) initially fall into the *trans-perp* well. Once the internal energy of the HOONO molecules is below the isomerization barrier, vibrational energy is equilibrated with translations on a microsecond time scale under our experimental conditions. This initial yield of vibrationally thermalized HOONO isomers depends critically on the relative density of states of the two isomers just above the top of the barrier at low pressures. At higher pressures, collisional relaxation may become competitive with isomerization rates.

After the HOONO molecules relax to an initial *c-c/t-p* population, the *trans-perp* HOONO isomerize on a slower time scale of 0.1–10 ms (over the temperature range of interest), and the *c-c/t-p* populations approach thermal equilibrium. Using the 11.4 kcal/mol barrier for the *cis-cis* to *trans-perp* isomerization and the 3.4 kcal/mol energy separation between the isomers (both zero-point corrected) and assuming a doubly degenerate reaction path, we find isomerization lifetimes of 0.35 ms and 1.5 ms at 300 and 260 K, respectively. Even with a zero-point corrected *perp-perp* energy of 13.5 kcal/mol and assuming a single reaction path, the lifetime for *trans-perp* relative to isomerization was 18 ms at 300 K. Thus, *trans-perp* HOONO is expected to convert to the lowest energy conformer rapidly relative to the characteristic residence time of products in the flow cell (200 ms). Therefore, the initial yields of the HOONO isomers from  $\text{OH} + \text{NO}_2 + \text{M}$ , which are difficult to compute, will not be detected in our experiment.

## Discussion

**A. Total HOONO Yield.** The current experiment measures the branching ratio for the formation of one HOONO isomer, the lowest energy *cis-cis* conformation, relative to formation of nitric acid. These results thus put a rigorous lower bound on the total HOONO yield, as other isomers of HOONO may have been formed but were undetected.

Two other HOONO isomers have been predicted, both with OH stretch bands that would overlap with that of nitric acid. Recent calculations conclude that the second lowest energy form, the *cis-perp* isomer, is an inflection point, not a minimum, along the torsional potential about the peroxy bond. This result is consistent with the absence of spectroscopic evidence for the *cis-perp* isomer in matrixes. We consider first the possible formation of the *trans-perp* isomer, whose energy is predicted to be  $\Delta E_0 = +3.4$  kcal/mol relative to the *cis-cis* isomer, and then briefly discuss possible problems arising from torsionally excited *cis-cis* HOONO.

Any *trans-perp* HOONO products formed by reaction 2 would most likely isomerize to the *cis-cis* form, because the computed isomerization barrier (11.4 kcal/mol) is predicted to be much lower than the dissociation threshold (18.3 kcal/mol). The absence of any change in the *cis-cis* HOONO abundance with residence time is consistent with one of three hypotheses: (a) the *trans-perp* form equilibrates rapidly with *cis-cis*, prior to entry into the detection volume, (b) no *trans-perp* isomer is formed, or (c) the *trans-perp* isomer isomerizes very slowly compared to the residence time.

Our RRKM calculations with MultiWell support the first scenario, that *trans-perp* isomers rearrange rapidly and are in equilibrium with *cis-cis* HOONO in the detection volume. We calculate that the rate is  $> 10^3 \text{ s}^{-1}$  at room temperature, and is sufficiently fast, even if the zero-point corrected barrier is as high as 13.5 kcal/mol. Furthermore, the calculations assume that the *perp-perp* conformation is the only transition state, but other pathways may exist.

If isomerization of the *trans-perp* isomer to the *cis-cis* form is indeed rapid compared to the residence time, we can calculate the total yield of HOONO in reactions 1 and 2. From the energetics and frequencies predicted by our CCSD(T) calculations in Table 2, we find  $K_{\text{eq}}(300 \text{ K}) = [\textit{trans-perp} \text{ HOONO}] / [\textit{cis-cis} \text{ HOONO}] = 0.005$ . Thus, at equilibrium only a negligible fraction the HOONO will be in the *trans-perp* conformation. Even at the highest temperature reported here, the *trans-perp* isomer contributes less than 1.5% to the total population at equilibrium.

While the *cis-perp* isomer is not bound in CCSD(T) calculations,<sup>46</sup> its geometry may be accessed by low ( $\nu_9 \geq 1$ ) torsional levels of the NOOH torsion. This torsional motion breaks the intramolecular hydrogen bond, and the large predicted change in the OH vibrational frequency with torsional angle suggests that the sequence bands involving  $\nu_9$  will be significantly blue-shifted. The excited torsional modes—which may account for 10–30% of the *cis-cis* HOONO population—may be the cause of the intensity on the blue side of the spectrum in Figure 5. However, we cannot rule out that some of the sequence bands cannot be detected within the  $3306 \text{ cm}^{-1}$  band. Thus, the observed yield obtained from the integrated absorbance of the  $3306 \text{ cm}^{-1}$  band may underestimate the HOONO yield, though by at most 10–30%. Only detailed modeling of the torsional levels with accurate ab initio potentials, or direct observation of the sequence bands, will allow us to settle this question.

We conclude that the observed *cis-cis* yield accounts for essentially all HOONO formed, i.e., that  $k_2/k_1 = 0.075$  at 20 Torr and 300 K for the reaction  $\text{OH} + \text{NO}_2 + \text{M}$ .

**B. Comparison with Previous Measurements.** Both Burkholder et al. and Dransfield et al. were unable to detect HOONO by FT-IR spectroscopy. Burkholder et al. placed an upper limit of 5% on the HOONO yield,<sup>51</sup> but assumed equal  $\nu_1$  cross sections with nitric acid; if our CCSD(T) intensities are used, this upper limit becomes 14%. Our yield also agrees with their HONO<sub>2</sub> yield of 75% + 25%–10% determined from mass balance. Dransfield et al. scanned a wider spectral range under a variety of conditions;<sup>52</sup> they reported an estimate from the mass balance of the HOONO yield to be  $0.0 \pm 4.1\%$  at 298 K and 60 Torr. Curiously, their published spectra end at  $3200 \text{ cm}^{-1}$ . Our experiments suggest that the concentrations of HOONO in their experiments were near the limits of the reported sensitivities. In addition, their measurements were performed at higher pressures, where HOONO yields may be higher but collisional dissociation will be faster.

Nizkorodov and Wennberg<sup>54</sup> reported a HOONO yield of  $5 \pm 3\%$  at 253 K and 20 Torr. These measurements were performed under conditions similar to our own, but were based on detection of HOONO alone. Their uncertainty arose because the authors assumed that the HOONO overtone cross-sections were the same as that of HO<sub>2</sub>NO<sub>2</sub>, and that HOONO dissociated with unit quantum efficiency. There was also some uncertainty in the assignment of the peaks, as no rotational structure was resolved. They assigned peaks in a cluster of bands to the  $\nu_1$  overtones of the *cis-cis*, *cis-perp*, and *trans-perp* isomers; more recent results<sup>82</sup> suggest that these are all combination bands, hot bands, and/or Fermi resonances of the *cis-cis* isomer. Given these assumptions, their yield is in quite good agreement with the current findings.

Donahue et al. estimated a low-pressure branching ratio of 0.17 from their isotope exchange measurements, but this estimate is rather weakly constrained by data.<sup>53</sup> Furthermore, since the high-pressure data had not been corrected, they

consequently overestimated  $k_2^{\text{ex}}$  for HOONO, and this discrepancy will have had an impact on their low-pressure extrapolation.

Hippler et al. measured a high-pressure branching ratio in He of 0.33 at 430 K, which fell to 0.15 at 5 bar He.<sup>32</sup> Since HOONO yields are predicted to be further reduced at lower pressures, these results are qualitatively consistent with the present data. They did not estimate rate constants in the low-pressure limit, so a direct comparison would require the pressure and temperature dependences.

Comparisons with the earlier modeling results are more tenuous, since the calculations are sensitive to input parameters. Troe's calculation,<sup>34</sup> for example, may have underestimated the HOONO yield by using too low a binding energy. Matheu and Green<sup>33</sup> attempted to model both forms of HOONO; they find the low-pressure ratio  $k_2/k_1 \geq 0.02$ . Our results are in good agreement with Golden and Smith,<sup>31</sup> who predict  $k_2/k_1 = 0.1$  in the low-pressure limit; this rate was arrived at by multiplying the computed *cis-cis* rate by three to account for the three isomers. Our results are in satisfactory agreement with recent work by Golden, Barker, and Lohr,<sup>35</sup> the most detailed master equation modeling calculations to date. From their fitted parameters, we compute a branching ratio of 0.057 at 13 Torr of N<sub>2</sub>.

**C. Atmospheric Implications.** The low-pressure branching ratios reported here provide an important constraint on the low-pressure  $k_2^0/k_1^0$  branching ratio for models, and are a lower limit on HOONO yields in the atmosphere. The gas mixture, He:Ar:N<sub>2</sub>, at 20 Torr is equivalent to approximately 13 Torr of dry air after collision efficiencies  $\beta$  of the gases are taken into account. The HOONO yield at pressures relevant to the atmosphere will be higher than the yields reported here. Doubling or tripling of this yield could significantly affect atmospheric models. However, while calculations predict that HOONO yields will increase to high levels at atmospheric pressures, one cannot yet predict with full confidence the true falloff curves for HOONO.

Laboratory measurements of reaction 1 generally detect only loss of reactants (typically OH under pseudo-first-order conditions); however, the reported rate coefficient may be either  $k_1$  or  $(k_1 + k_2)$ , depending on whether HOONO has collisionally dissociated on the time scale of the measurements. The implications of the current branching ratio will then depend on the specific experiment.

## Conclusions

This work establishes the formation of HOONO as a minor product channel in the reaction OH + NO<sub>2</sub>, consistent with recent experimental observations by Donahue,<sup>53</sup> Nizkorodov,<sup>54</sup> and Hippler.<sup>32</sup> Our experiments unambiguously identify HOONO by mid-infrared spectroscopy and provide a direct measure of the branching ratio in the temperature range 270–360 K. We have exploited the sensitive technique of cavity ringdown spectroscopy to detect the absorption spectrum of the  $\nu_1$  band of *cis-cis* HOONO, centered at 3306 cm<sup>-1</sup>. The rotational envelope, obtained after subtracting the contributions from the neighboring HONO  $\nu_2$  overtones, agrees well with the simulated spectrum derived from high-level *ab initio* calculations. We determined the HOONO:HONO<sub>2</sub> product branching ratio  $k_2/k_1$  for the OH + NO<sub>2</sub> + M reaction as a function of reaction pressure and temperature from measurements of the integrated absorption of the  $\nu_1$  bands of *cis-cis* HOONO and HONO<sub>2</sub>. These measurements were converted to branching ratios using the ratio of calculated integrated intensities of HOONO and HONO<sub>2</sub> bands at the CCSD(T)/cc-pVTZ level. The use of

computed cross sections leads to the largest contribution to the uncertainty in the branching ratio. We find a branching ratio of  $k_2/k_1 = 0.075 \pm 0.020(2\sigma)$  at room temperature and 20 Torr (He/Ar/N<sub>2</sub> buffer gas). This branching ratio decreases weakly with increasing temperature over the range 270–360 K. Although a second isomer of HOONO may be formed, statistical rate calculations show that the higher energy conformer, *trans-perp* HOONO, is expected to isomerize rapidly on the time scale of the current experiment, and will be in its equilibrium abundance, computed to be < 1.5% of the total population. A small fraction of  $\nu_9$  (HOON-torsion) excited molecules that access the *cis-perp* geometry may have sequence bands that are significantly blue-shifted and lie under the HONO<sub>2</sub> band, and thus be undetected. Thus, the current measurements provide a firm lower bound for and may be a good estimate of the total yield of HOONO.

**Acknowledgment.** This work was supported by NASA Grants NAG5-11657 and NAGW-3911 and the Upper Atmospheric Research and Tropospheric Chemistry Programs. A.K.M. acknowledges support of an NSF Graduate Research Fellowship, G.N. support by a Caltech SURF Fellowship, and G.N. and S.A.N. by the Camille and Henry Dreyfus Postdoctoral Program in Environmental Chemistry. Calculations were supported by the NASA JPL Supercomputing Project. We thank D. M. Golden and J. R. Barker for sharing their results prior to publication and A. Goldman for providing spectral data.

## References and Notes

- Perkins, K. K.; Hanisco, T. F.; Cohen, R. C.; Koch, L. C.; Stimpfle, R. M.; Voss, P. B.; Bonne, G. P.; Lanzendorf, E. J.; Anderson, J. G.; Wennberg, P. O.; Gao, R. S.; Del Negro, L. A.; Salawitch, R. J.; McElroy, C. T.; Hantsa, E. J.; Loewenstein, M.; Bui, T. P. *J. Phys. Chem. A* **2001**, *105*, 1521.
- Seinfeld, J. H.; Pandis, S. N. *Atmospheric Chemistry and Physics: From Air Pollution to Climate Change*; 1998.
- Gao, D. F.; Stockwell, W. R.; Milford, J. B. *J. Geophys. Res.-D* **1996**, *101*, 9107.
- Gao, D. F.; Stockwell, W. R.; Milford, J. B. *J. Geophys. Res.-D* **1995**, *100*, 23153.
- Tonnesen, G. S. *Atmos. Env.* **1999**, *33*, 1587.
- Yang, Y. J.; Stockwell, W. R.; Milford, J. B. *Environ. Sci. Technol.* **1995**, *29*, 1336.
- Bergin, M. S.; Russell, A. G.; Milford, J. B. *Environ. Sci. Technol.* **1998**, *32*, 694.
- Smith, G. P.; Dubey, M. K.; Kinnison, D. E.; Connell, P. S. *J. Phys. Chem. A* **2001**, *105*, 1449.
- Robertshaw, J. S.; Smith, I. W. M. *J. Phys. Chem.* **1982**, *86*, 785.
- Westenberg, A. A.; DeHaas, N. *J. Chem. Phys.* **1972**, *57*, 5375.
- Anderson, J. G.; Kaufman, F. *Chem. Phys. Lett.* **1972**, *16*, 375.
- Anderson, J. G.; Margitan, J. J.; Kaufman, F. *J. Chem. Phys.* **1974**, *60*, 3310.
- Harris, G. W.; Wayne, R. P. *J. Chem. Soc., Faraday Trans. 1* **1975**, *71*, 610.
- Howard, C. J.; Evenson, K. M. *J. Chem. Phys.* **1974**, *61*, 1943.
- Morley, C.; Smith, I. W. M. *J. Chem. Soc., Faraday Trans. 2* **1972**, *68*, 1016.
- Anastasi, C.; Bemand, P. P.; Smith, I. W. M. *Chem. Phys. Lett.* **1976**, *37*, 370.
- Anastasi, C.; Smith, I. W. M. *J. Chem. Soc., Faraday Trans. 2* **1976**, *72*, 1459.
- Atkinson, R.; Perry, R. A.; Pitts, J. N., Jr. *J. Chem. Phys.* **1976**, *65*, 306.
- Wine, P. H.; Kreutter, N. M.; Ravishankara, A. R. *J. Phys. Chem.* **1979**, *83*, 3191.
- Troe, J. *J. Phys. Chem.* **1979**, *83*, 114.
- Forster, R.; Frost, M.; Fulle, D.; Hamann, H. F.; Hippler, H.; Schlegel, A.; Troe, J. *J. Chem. Phys.* **1995**, *103*, 2949.
- Donahue, N. M.; Dubey, M. K.; Mohrschladt, R.; Demerjian, K. L.; Anderson, J. G. *J. Geophys. Res. D* **1997**, *102*, 6159.
- Donahue, N. M.; Demerjian, K. L.; Anderson, J. G. *J. Phys. Chem.* **1996**, *100*, 17855.
- Fulle, D.; Hamann, H. F.; Hippler, H.; Troe, J. *J. Chem. Phys.* **1998**, *108*, 5391.

- (25) Brown, S. S.; Talukdar, R. K.; Ravishankara, A. R. *Chem. Phys. Lett.* **1999**, *299*, 277.
- (26) D'Ottone, L.; Campuzano-Jost, P.; Bauer, D.; Hynes, A. J. *J. Phys. Chem. A* **2001**, *105*, 10538.
- (27) DeMore, W. B.; Sander, S. P.; Golden, D. M.; Hampson, R. F.; Kurylo, M. J.; Howard, C. J.; Ravishankara, A. R.; Kolb, C. E.; Molina, M. J. *Chemical Kinetics and Photochemical Data for Use in Stratospheric Modeling: Evaluation Number 12*. Jet Propulsion Laboratory, 1997.
- (28) Atkinson, R.; Baulch, D. L.; Cox, R. A.; Hampson, R. F.; Kerr, J. A.; Rossi, M. J.; Troe, J. *J. Chem. Phys. Ref. Data* **1997**, *26*, 1329.
- (29) Atkinson, R.; Baulch, D. L.; Cox, R. A.; Crowley, J. N.; Hampson, R. F.; Kerr, J. A.; Rossi, M. J.; Troe, J. *Evaluated kinetic and photochemical data for atmospheric chemistry. In IUPAC subcommittee on gas kinetic data evaluation for atmospheric chemistry*, 2002.
- (30) Leighton, P. A. *Photochemistry of air pollution*; Academic Press: New York, 1961.
- (31) Golden, D. M.; Smith, G. P. *J. Phys. Chem. A* **2000**, *104*, 3991.
- (32) Hippler, H.; Nasterlack, S.; Striebel, F. *Phys. Chem. Commun. Phys.* **2002**, *4*, 2959.
- (33) Matheu, D. M.; Green, W. H., Jr. *Int. J. Chem. Kinet.* **2000**, *32*, 245.
- (34) Troe, J. *Int. J. Chem. Kinet.* **2001**, *33*, 878.
- (35) Golden, D. M.; Barker, J. R.; Lohr, L. L. *J. Phys. Chem. A*, submitted.
- (36) McGrath, M. P.; Francl, M. M.; Rowland, F. S.; Hehre, W. J. *J. Phys. Chem.* **1988**, *92*, 5352.
- (37) McGrath, M. P.; Rowland, F. S. *J. Phys. Chem.* **1994**, *98*, 1061.
- (38) Tsai, H. H.; Hamilton, T. P.; Tsai, J. H. M.; vanderWoerd, M.; Harrison, J. G.; Jablonsky, M. J.; Beckman, J. S.; Koppenol, W. H. *J. Phys. Chem.* **1996**, *100*, 15087.
- (39) Sumathi, R.; Peyerimhoff, S. D. *J. Chem. Phys.* **1997**, *107*, 1872.
- (40) Doclo, K.; Rothlisberger, U. *Chem. Phys. Lett.* **1998**, *297*, 205.
- (41) Chakraborty, D.; Park, J.; Lin, M. C. *Chem. Phys.* **1998**, *231*, 39.
- (42) Jitariu, L. C.; Hirst, D. M. *Phys. Chem. Commun. Phys.* **1999**, *1*, 983.
- (43) Li, Y.; Francisco, J. S. *J. Chem. Phys.* **2000**, *113*, 7976.
- (44) Dixon, D. A.; Feller, D.; Zhan, C.-G.; Francisco, J. S. *J. Phys. Chem. A* **2002**, *106*, 3191.
- (45) Houk, K. N.; Condroski, K. R.; Pryor, W. A. *J. Am. Chem. Soc.* **1996**, *118*, 13002.
- (46) Francisco, J. S. Unpublished results.
- (47) Cheng, B. M.; Lee, J. W.; Lee, Y. P. *J. Phys. Chem.* **1991**, *95*, 2814.
- (48) Chen, W. J.; Lo, W. J.; Cheng, B. M.; Lee, Y. P. *J. Chem. Phys.* **1992**, *97*, 7167.
- (49) Lo, W.-J.; Lee, Y. *J. Chem. Phys.* **1994**, *101*, 5494.
- (50) Koch, T. G.; Sodeau, J. R. *J. Phys. Chem.* **1995**, *99*, 10824.
- (51) Burkholder, J. B.; Hammer, P. D.; Howard, C. J. *J. Phys. Chem.* **1987**, *91*, 2136.
- (52) Dransfield, T. J.; Donahue, N. M.; Anderson, J. G. *J. Phys. Chem. A* **2001**, *105*, 1507.
- (53) Donahue, N. M.; Mohrschladt, R.; Dransfield, T. J.; Anderson, J. G.; Dubey, M. K. *J. Phys. Chem. A* **2001**, *105*, 1515.
- (54) Nizkorodov, S. A.; Wennberg, P. O. *J. Phys. Chem. A* **2002**, *106*, 855.
- (55) Lo, W.-J.; Lee, Y. P. *J. Chem. Phys.* **1994**, *101*, 5494.
- (56) Irvine, A. M. L.; Smith, I. W. M.; Tuckett, R. P.; Yang, X. F. *J. Chem. Phys.* **1990**, *93*, 3177.
- (57) O'Keefe, A.; Deacon, D. A. G. *Rev. Sci. Instrum.* **1988**, *59*, 2544.
- (58) Berden, G.; Peeters, R.; Meijer, G. *Int. Rev. Phys. Chem.* **2000**, *19*, 565.
- (59) Brown, S. S.; Wilson, R. W.; Ravishankara, A. R. *J. Phys. Chem.* **2000**, *104*, 4976.
- (60) Reid, S. A.; Tang, Y. *Appl. Opt.* **1996**, *35*, 1473.
- (61) Press, W. H.; Teukolsky, W. T.; Vetterling, W. T.; Flannery, B. P. *Numerical Recipes in Fortran*, 2nd ed.; Cambridge University Press: Cambridge, 1992.
- (62) O'Keefe, A.; Deacon, D. A. G. *Rev. Sci. Instrum.* **1988**, *59*, 2544.
- (63) Zalicki, P.; Zare, R. N. *J. Chem. Phys.* **1995**, *102*, 2708.
- (64) Romanini, D.; Lehmann, K. K. *J. Chem. Phys.* **1993**, *99*, 6287.
- (65) Lange, K. R.; Wells, N. P.; Plegge, K. S.; Phillips, J. A. *J. Phys. Chem. A* **2001**, *105*, 3481.
- (66) Frisch, M. J.; Trucks, G. W.; Schlegel, H. B.; Scuseria, G. E.; Robb, M. A.; Cheeseman, J. R.; Zakrzewski, V. G.; Montgomery, J. A., Jr.; Stratmann, R. E.; Burant, J. C.; Dapprich, S.; Millam, J. M.; Daniels, A. D.; Kudin, K. N.; Strain, M. C.; Farkas, O.; Tomasi, J.; Barone, V.; Cossi, M.; Cammi, R.; Mennucci, B.; Pomelli, C.; Adamo, C.; Clifford, S.; Ochterski, J.; Petersson, G. A.; Ayala, P. Y.; Cui, Q.; Morokuma, K.; Malick, D. K.; Rabuck, A. D.; Raghavachari, K.; Foresman, J. B.; Cioslowski, J.; Ortiz, J. V.; Stefanov, B. B.; Liu, G.; Liashenko, A.; Piskorz, P.; Komaromi, I.; Gomperts, R.; Martin, R. L.; Fox, D. J.; Keith, T.; Al-Laham, M. A.; Peng, C. Y.; Nanayakkara, A.; Gonzalez, C.; Challacombe, M.; Gill, P. M. W.; Johnson, B. G.; Chen, W.; Wong, M. W.; Andres, J. L.; Head-Gordon, M.; Replogle, E. S.; Pople, J. A. *Gaussian 98*, A.10 ed.; Gaussian, Inc.: Pittsburgh, PA, 2001.
- (67) Werner, H. J.; Knowles, P. J. "MOLPRO is a package of ab initio programs written with contributions from J. Almlöf, R. D. Amos, A. Bernhardsson, A. Berning, P. Celani, D. L. Cooper, M. J. O. Deegan, A. J. Dobbyn, F. Eckert, S. T. Elbert, C. Hampel, G. Hetzer, T. Korona, R. Lindh, A. W. Lloyd, S. J. McNicholas, F. R. Manby, W. Meyer, M. E. Mura, A. Nicklass, P. Palmieri, K. A. Peterson, R. M. Pitzer, P. Pulay, G. Rauhut, M. Schütz, H. Stoll, A. J. Stone, R. Tarroni, P. R. Taylor, T. Thorsteinsson," University of Sussex, 2000.
- (68) Raghavachari, K.; Trucks, G. W.; Pople, J. A.; Head-Gordon, M. *Chem. Phys. Lett.* **1989**, *157*, 479.
- (69) Pople, J. A.; Head-Gordon, M.; Raghavachari, K. *J. Chem. Phys.* **1987**, *87*, 5968.
- (70) Lee, T. J.; Rendell, Taylor, P. R. *J. Phys. Chem.* **1990**, *94*, 5463.
- (71) Dunning, T. H., Jr. *J. Chem. Phys.* **1989**, *90*, 1007.
- (72) Kendall, R. A.; Dunning, T. H., Jr.; Harrison, R. J. *J. Chem. Phys.* **1992**, *96*, 6796.
- (73) Martin, J. M. L. *J. Chem. Phys.* **1999**, *100*, 8186.
- (74) Bartlett, R. J.; Stanton, J. F. In *Reviews of Computational Chemistry*; Lipkowitz, K. B.; Boyd, D. B., Eds.; VCH Publishers: New York, 1994; Vol. 5, p 65.
- (75) Barker, J. R. *Int. J. Chem. Kinet.* **2001**, *33*, 232.
- (76) Barker, J. R. "MultiWell-1.3.1 software," 2003.
- (77) Galabov, B.; Yamaguchi, Y.; Remington, R. B.; Schaefer, H. F. I. *J. Phys. Chem.* **2002**, *106*, 819.
- (78) Thomas, J. R.; DeLeeuw, B. J.; Vacek, G.; Crawford, T. D.; Yamaguchi, Y.; Schaefer, H. F. I. *J. Chem. Phys.* **1993**, *99*, 403.
- (79) Judge, R. H.; Clouthier, D. J. *Comput. Phys. Commun.* **2001**, *135*, 293.
- (80) Guilmot, J. M.; Melen, F.; Herman, M. *J. Mol. Spectrosc.* **1993**, *160*, 401.
- (81) Guilmot, J. M.; Godefroid, M.; Herman, M. *J. Mol. Spectrosc.* **1993**, *160*, 387.
- (82) Fry, J.; Nizkorodov, S. A.; Okumura, M.; Wennberg, P. O. In preparation.
- (83) Yalin, A. P.; Zare, R. N. *Laser Phys.* **2002**, *12*, 1065.
- (84) Hodges, J. T.; Looney, J. P.; van Zee, R. D. *Appl. Opt.* **1996**, *35*, 4112.
- (85) Goldman, A.; Rinsland, C.; Perrin, A.; Flaud, J. M. *J. Quant. Spectrosc. Radiat. Transfer* **1998**, *60*, 351.
- (86) Mollner, A. K.; Nair, G.; Sander, S. P.; Okumura, M. In preparation.
- (87) May, R. D.; Friedl, R. R. *J. Quant. Spectrosc. Radiat. Transfer* **1993**, *50*, 257.

## 5.2 Revisions to Branching-Ratio Results

As described in chapters 2 and 3, our understanding of the spectroscopy used to measure the branching ratio has improved since these results were published. This section briefly describes what revisions should be made to the published data.

The smallest correction is to the calculated ratio of cross sections used. More recent calculations taking into account anharmonicities indicate that this should be changed from 2.87 to 2.71 [73, 74].

Since the publication of Bean et al. we have a much improved understanding of the *cis-cis* HOONO spectrum. In particular, we understand that there is considerable OH stretch intensity blueshifted outside the main peak we used to measure the HOONO absorbance. As described in Chapter 3, our observed HOONO absorbances should have been multiplied by 1.41 to correct for this.

Our assumed correction for nonlinearities in the nitric acid absorbance was significantly too small. We had assumed we could correct our observed nitric acid absorbances by multiplying them by 1.2. As described in detail in Chapter 2, at the low pressures of these experiments we should instead have multiplied by 2.5.

As a result, the Bean et al. results should be corrected using

$$\text{BR}_{\text{new}} = \text{BR}_{\text{published}} \times \frac{2.71}{2.87} \times \frac{1.2}{2.5} \times 1.41 = \text{BR}_{\text{published}} \times 0.64.$$

The branching ratio at 298K and 13 torr is thus revised from  $k_2(c-c)/k_1 = 0.075 \pm 0.020$  to  $k_2(c-c)/k_1 = 0.048 \pm 0.013$ . A revised version of Figure 6 from Bean et al. is shown below.

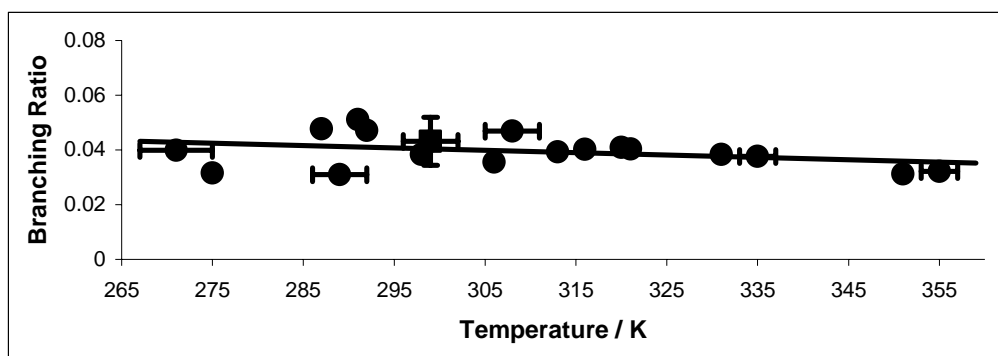


Figure 5.1 – Corrected ratio of *cis-cis* to HONO<sub>2</sub> products in the reaction of OH + NO<sub>2</sub> as a function of temperature, at 20 Torr.

## **6 Appendix B: Experimental Details**

### ***6.1 Room Temperature Photolysis Cells***

Machine drawings are included of the Teflon blocks and photolysis cells used in photolysis-initiated CRDS studies described in Chapters 4 and 5. Teflon block drawings are courtesy of Brian Bean and were submitted to the machine shop for fabrication. The blocks were coupled to the purge tubes and vacuum line via stainless steel Ultratorr fittings threaded into the Teflon. Initial leaks at the stainless/Teflon interface were sealed by a generous helping of Teflon thread tape. The blocks were coupled to the gas inlet and pressure gauges by Teflon Swagelock fittings, also threaded into the blocks. These generally seal well, although the Teflon Swagelock parts wear down over the course of repeated tightenings. The seal between the Teflon blocks and the photolysis cell was the most problematic. This was accomplished by fitting the photolysis cells into square grooves in the Teflon blocks and pressing the Teflon blocks together. Often it was found that inserting silicon gaskets between the cell and the Teflon block could improve the seal. With nothing holding the gaskets out they would often deform and be pulled in by the vacuum, breaking the seal. Over time, the Teflon surrounding the square groove was deformed and pressed down into the groove. This made the square groove quite uneven and prevented a seal from being made.

Overall, the design of this cell was certainly functional. Once a good seal was made between the Teflon blocks and the photolysis cell, it would typically last until the cell need to be disassembled. Future cell designs may consider improving upon this seal

mechanism in one of two ways. A thin-walled stainless tube could be inserted inside the silicon gaskets to help them hold shape and resist deformation. This would have the disadvantage of reducing the inside diameter of the CRDS axis, which already can present difficulties for alignment. A compromise would have to be struck with the wall the tube weighing rigidity and inside diameter. The second solution would be to have a round plate welded to the end of the photolysis cells and then create an O-ring seal between this plate and the Teflon blocks. This would certainly seal quite well, but would have the disadvantage of creating significantly more volume containing precursors but not UV photons. This would increase the background for experiments such as the alkoxy experiments described in Chapter 4 and would require faster flow rates to accomplish the same flush duty cycle.

Name: Alkoxy Cell Assembly-2	Material: Teflon
Design: Brian Bean	Phone: x6014
Scale: 1:1	Units: Inches
	Pieces: 1

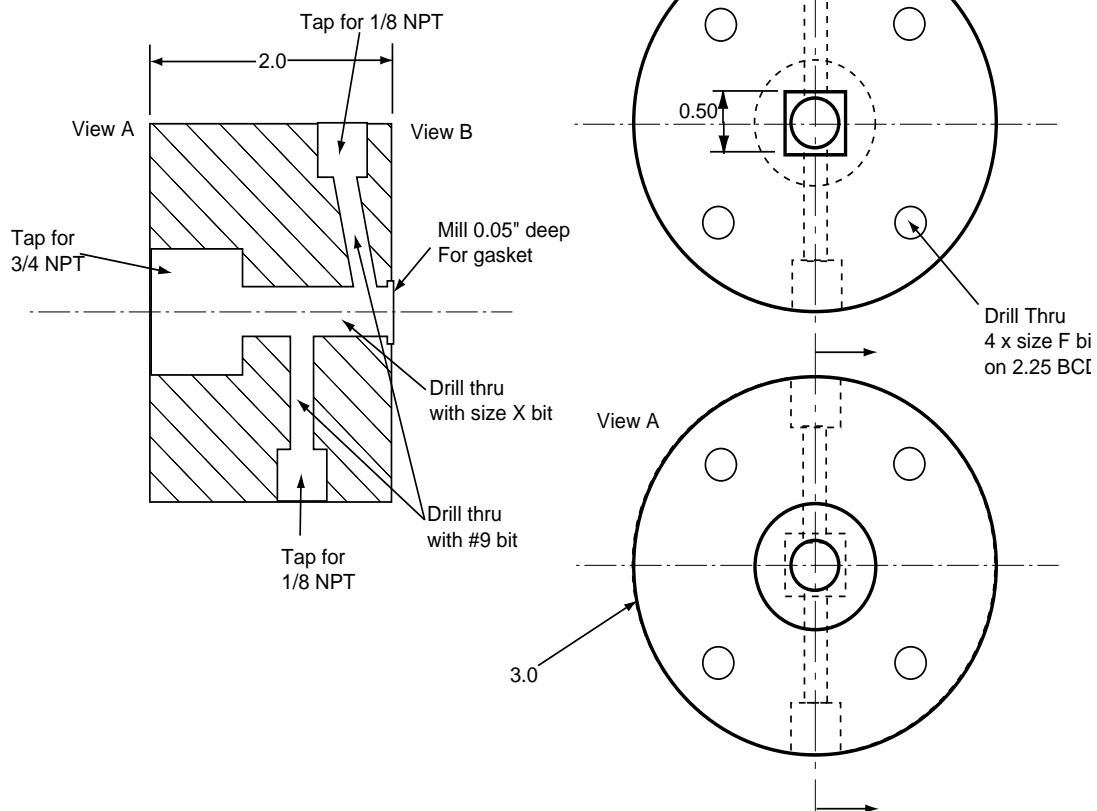


**Figure 6.1. Technical drawing for fabrication of Teflon block for coupling photolysis cell to CRDS mirrors and gas inlets.**

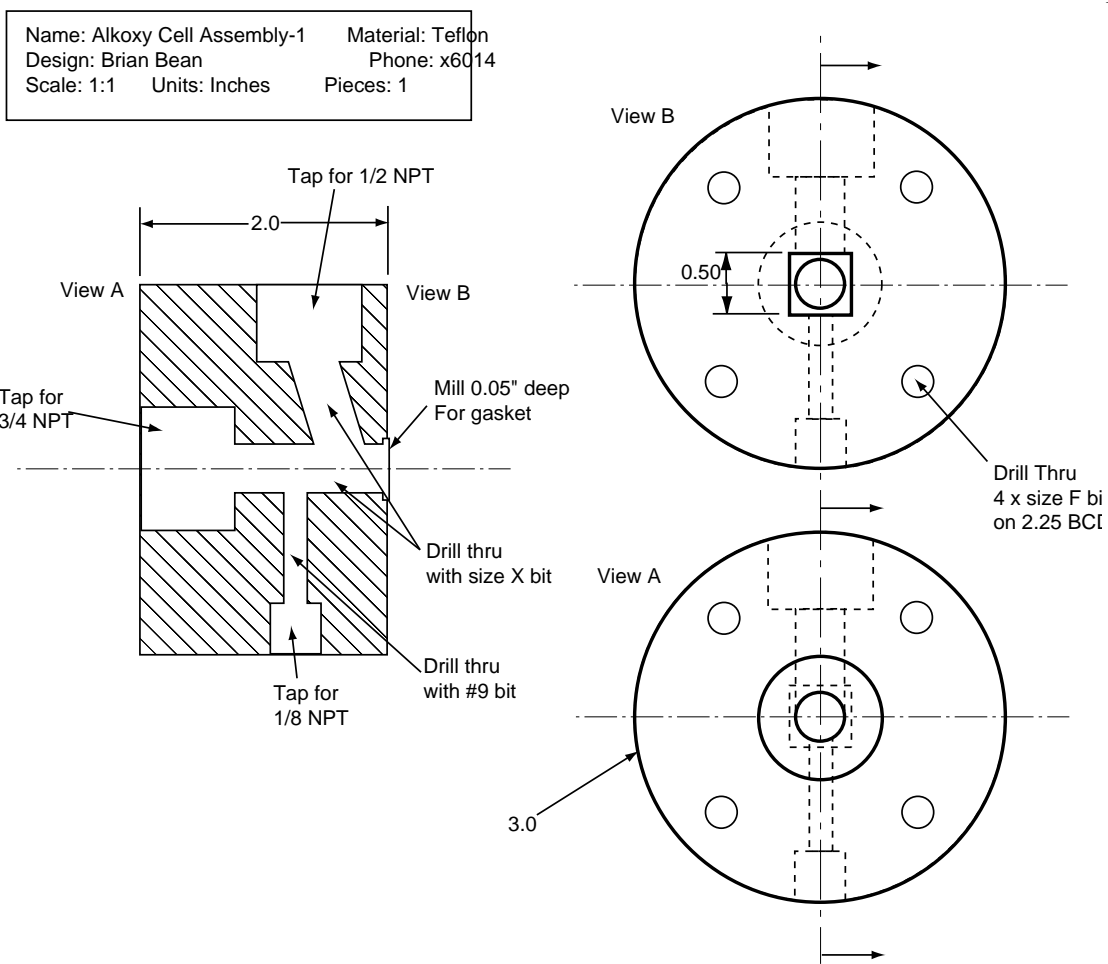


**Figure 6.2. Technical drawing for fabrication of Teflon block for coupling photolysis cell to CRDS mirrors and gas pumpout.**

Quartz Cell (Starna Cells: Quartz Fluorometer Cells 3-Q-10)



Stainless Steel Cells, Fabricated from 1-cm ID stainless square tubing.

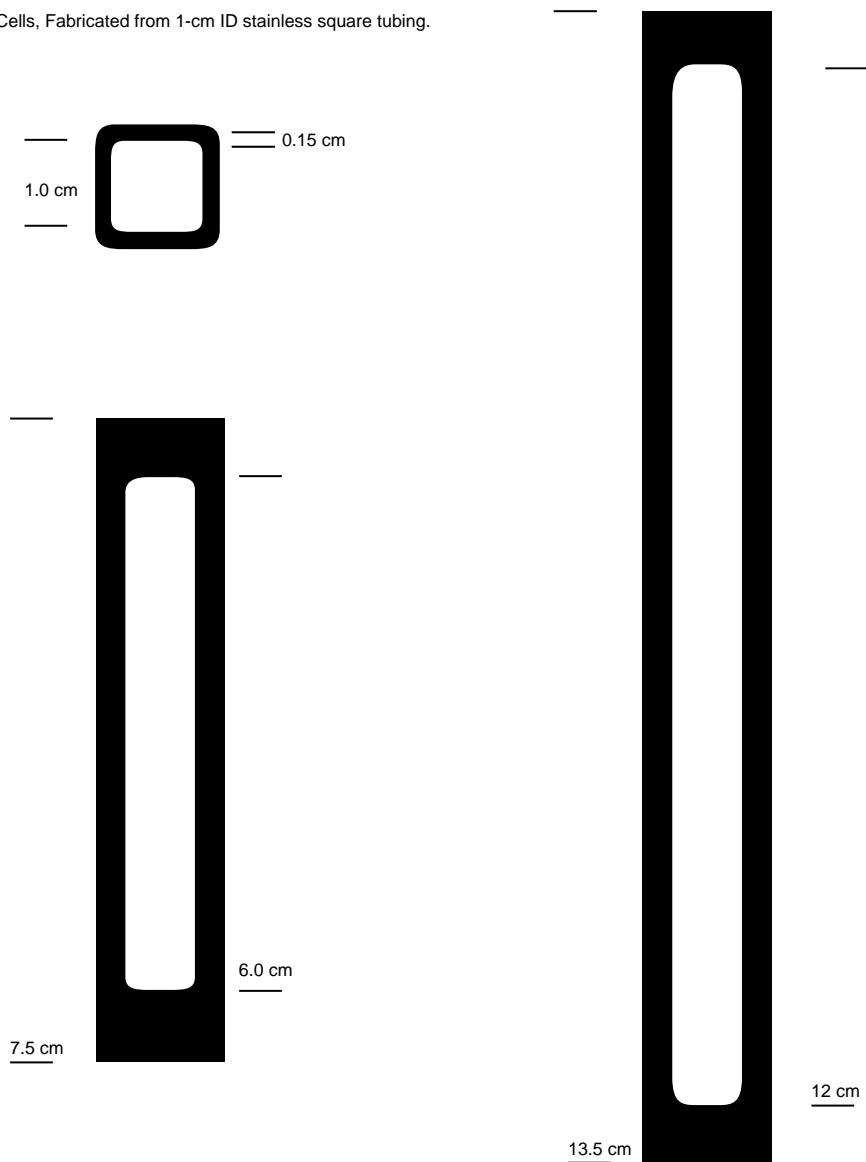


Figure 6.3. Diagrams of various photolysis cells used.

## 6.2 184.9 nm Intensity Measurements

The measurement of 184.9 nm intensities from a Hg lamp can be complicated by interference from other wavelengths. This section evaluates this possible interference for the experiments described in Chapter 2. These experiments used a mercury Pen-Ray lamp (UVP) to generate 184.9 nm light. As can be seen in Figure 6.4, these lamps produce many other wavelengths of light in addition to 184.9 nm.

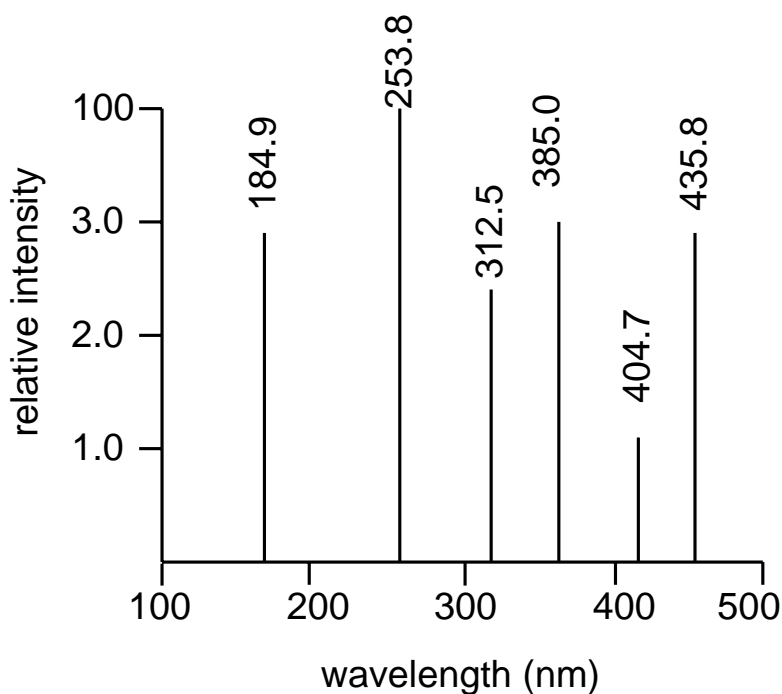
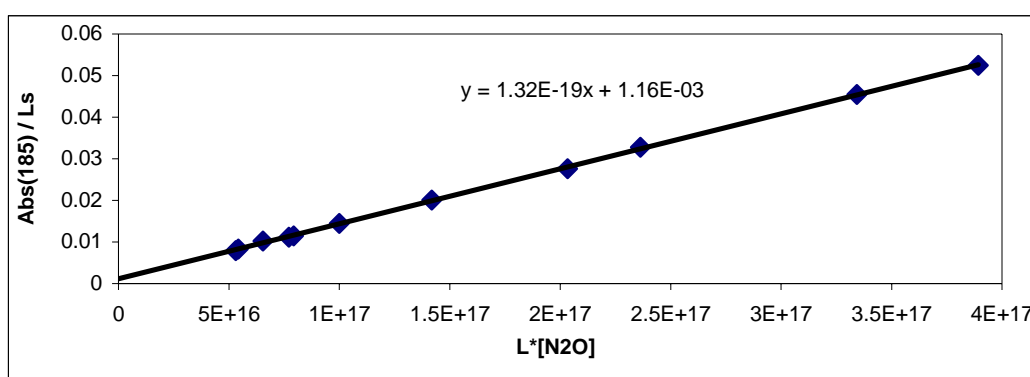


Figure 6.4. Stated relative line intensities for UVP Hg Pen-Ray lamp.

Intensity measurements were made with two slightly different detection apparatus. The original apparatus, used for measuring the nitric acid 185 nm cross section, consisted of two custom-made 185 nm interference filters and a PMT with a bi-alkali cathode. Our original concern when making these measurements was leakage from

the most intense emission line at 254 nm ( $I_{254} > 30 \cdot I_{185}$ ). This concern was addressed by filling the cell with a few hundred torr of  $N_2O$ . The cross sections at 185 nm and 254 nm are  $1.43 \times 10^{-19} \text{ cm}^2$  and  $< 10^{-23} \text{ cm}^2$  respectively. The resulting optical depths of  $> 30$  at 185 nm and  $< 0.01$  at 254 nm allowed for direct measurement of the 254 nm leakage:  $< 2\%$  of the total intensity. This contribution was subtracted from future measurements of the 185 nm intensity.



**Figure 6.5.** Fit to  $N_2O$  Beer's Law Absorbance w/ Hg lamp, double interference filter, and bialkali cathode.  $L_s = 30.2 \text{ cm}$ .

The Beer's Law absorption as a function of  $N_2O$  concentration, with the contribution from 254 nm leakage subtracted, is shown in Figure 6.5. The absorbance was linear over a wide range, and a linear fit to the data yielded an observed cross section of  $1.32 \times 10^{-19} \text{ cm}^2$ . This was about 5% below the literature cross section of  $1.43 \times 10^{-19} \text{ cm}^2$ . We were encouraged by the linearity of the plots and reproducibility of our measured cross section and felt this relatively small discrepancy was within the experimental uncertainty. Our measurements of the nitric acid 185 nm cross section as well as the initial measurements of the IR nitric acid integrated cross section were made using this same apparatus, subtracting the contribution from 254 nm leakage. Our initial linear fit to the data yielded a cross section of  $1.53 \times 10^{-17} \text{ cm}^2$ . Again, this was about 5%

lower than the accepted literature value [25]. This small discrepancy seemed reasonable, especially considering the scatter in nitric acid measurements at such short wavelengths [25-27, 29, 32, 33].

After we finished these initial measurements, the interference filters were lost. Aaron Noell at JPL then used the same for UV measurements of methanol in his cell. The double interference filters were replaced by a commercial 185 nm interference filter (Acton Research Corporation, 24 nm FWHM). Using the bialkali PMT, it was found that leakage by 194 nm light, a mercury emission line not listed in the UVP table shown in Figure 6.4, was an important photon contaminant. The predicted relative intensities (194:185 ratio taken from the CRC) convolved with the filter transmission properties are shown in Table 6.1. The expected relative intensities as observed by the PMT (after the filter) with a bialkali cathode, with fairly constant quantum efficiency, are shown in the column labeled “postfilter intensity.” We see that, despite the 194 nm intensity being much smaller than that at 254 nm, the 194 nm light is expected to be a much larger problem due to the properties of the filter. Aaron further reduced the contribution of 194 nm light by a factor of five by switching to a solar-blind CsI PMT. The resulting expected signal as seen by the CsI PMT is also shown in Table 6.1. We see that the contribution from non-185 nm light is expected to be about 5%. The values in Table 6.1 can only be trusted as a rough guide, though, as the specific output characteristics of Pen-Ray lamps vary from lamp to lamp and over the lifetime of the lamp.

**Table 6.1. Expected contribution of various Hg Pen-Ray lamp wavelengths. All values other than wavelengths are relative and unitless.**

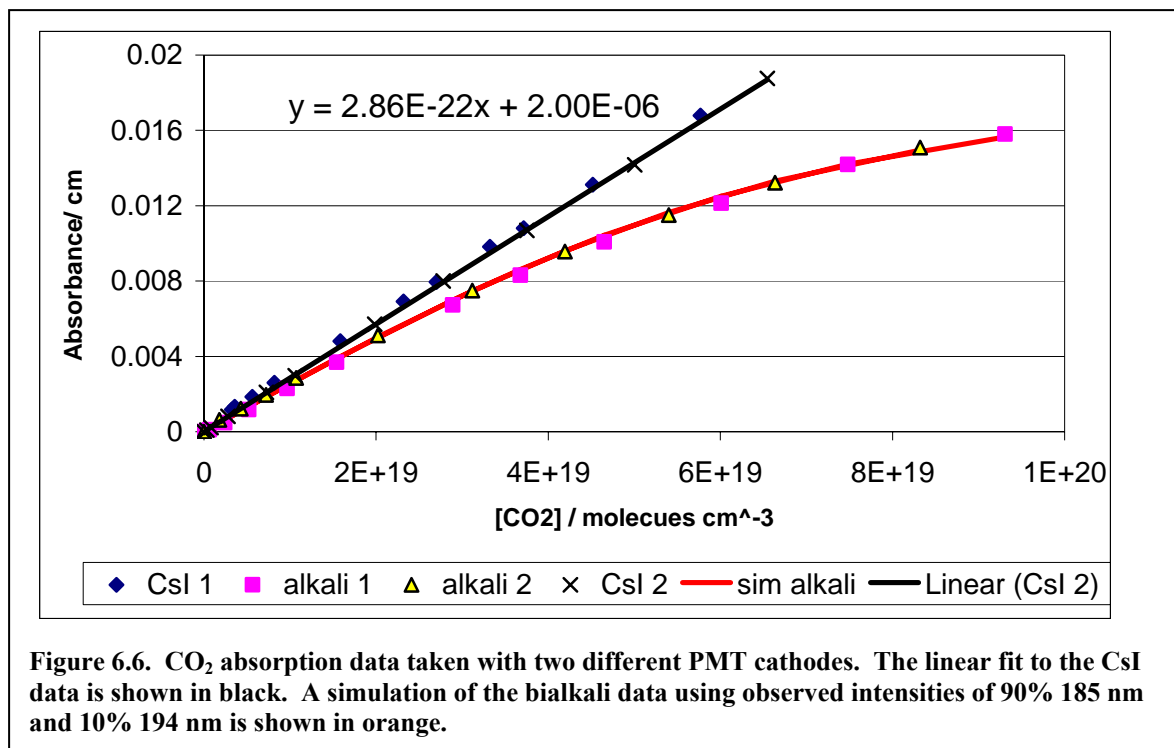
wavelength /nm	Intensity	Filter transmission	postfilter intensity	CsI Response	CsI Signal
184.95	1000	0.18	180	1	180
194.23	300	0.15	45	0.2	9
253.65	30000	0.0001	3	<0.2?	<0.6?

When we returned to IR integrated cross section measurements, we used the solar-blind CsI PMT that Aaron had used. Unfortunately, we did not re-measure the nitric acid UV cross section and so do not know if 194 nm contamination influenced this measurement. At the moment, the UV equipment necessary to re-measure this cross section is not available. Instead, I have tried to quantify the contribution of the 194 nm emission from the Pen-Ray lamp to our previous measurement of the nitric acid UV cross section.

The apparatus used was a 160 cm stainless steel Raman cell with UV-transparent windows. The Hg Pen-Ray lamp output was sent through a 10 cm focal length CaF<sub>2</sub> lens and a pinhole to collimate the light through the cell. A second pinhole was used at the output window to minimize the collection of photons that reflected within the cell. The same Acton Research 185 nm interference filter described above was used to drastically reduce the detection of 254 nm light. The PMT output was amplified and then sent to an oscilloscope for averaging. The pressure in the cell was measured by a 10K torr MKS Baratron. The experiments consisted of measuring the transmitted intensity as a function of CO<sub>2</sub> pressure using both the bialkali and CsI cathode in the PMT and then comparing

the absorbance as a function of pressure for the two.  $\text{CO}_2$  was chosen because  $\sigma_{185} = 13 \times \sigma_{194}$  and because the UV spectrum in this region lacks structure.

Absorbance data as a function of  $\text{CO}_2$  concentration are shown in Figure 6.6. The data taken with the CsI cathode appeared linear for the range of absorbances measured ( $\text{Abs} \leq 3$ ). The fit to this data is almost identical to the literature value of  $2.85 \times 10^{-22} \text{ cm}^2$  [105]. The data taken with the bialkali cathode show obvious curvature, even at absorbances below 0.5. The data can be simulated using only the cross sections at 185 nm and 194 nm. The simulation shown in Figure 6.6 assumes 90% 185 nm and 10% 194 nm and fits the data very well over the entire range of observed absorbances.



As Figure 6.6 demonstrates, 184.9 nm intensities taken with the CsI cathode and new filter were likely free from 194 nm contamination. While we cannot re-test the interference filters used in conjunction with the bi-alkali cathode directly, it is likely they

had similar transmission properties to the current filter. Making this assumption, we can use the relative contributions of 185 and 194 nm light derived from Figure 6.6 to correct the intensities measured while measuring  $\sigma_{185}$ . The observed intensities were therefore corrected to be that of just 185 by

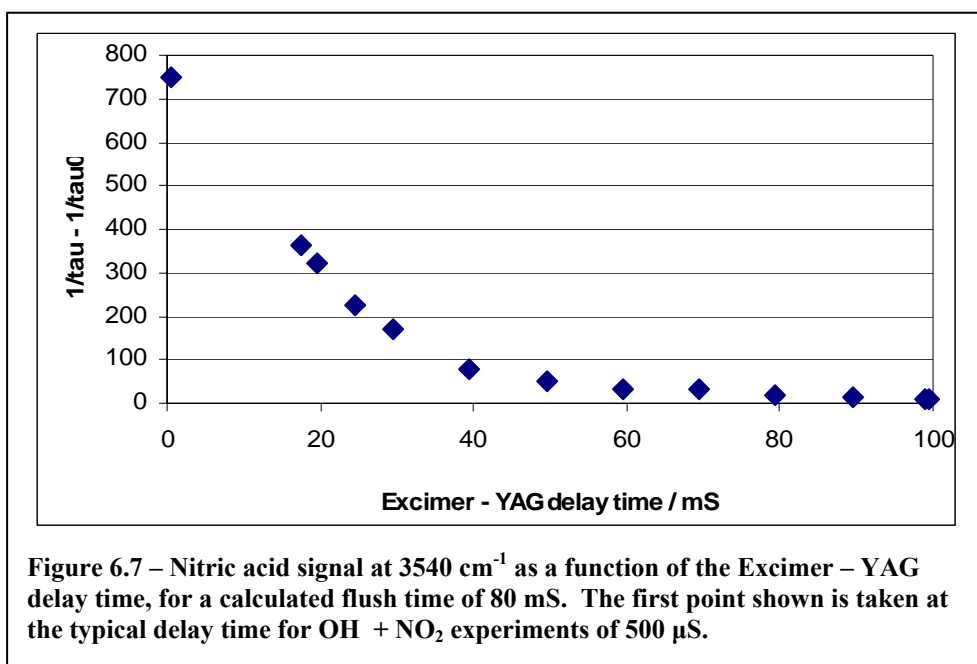
$$I_{185} = I_{obs} - \left[ I_{0,obs} \times 0.095 \times \exp(-\sigma_{194} \times I_s \times [\text{HNO}_3]) \right].$$

This led to very small changes ( $\approx 1\%$ ) in the intensities and only a 1% increase in our measured  $\sigma_{185}$ . Because we have had to assume the old filters had similar transmission properties to the new filter, this has been included as an uncertainty in the analysis of our  $\sigma_{185}$  measurements described in Section 2.2.2.

### 6.3 Flow Cell Flush Times

In photolysis experiments, it is important to ensure that a fresh gas sample is being photolyzed with each excimer pulse. In this way secondary chemistry and other potential problems stemming from the photolysis of products are eliminated. The group lore when I joined was that, if you calculate the flush time of the photolysis region of the flow cell from the pressure and flowmeter readouts, you should multiply that number by two to get the actual time for a clean gas sample. This was assumed to be the result of diffusion of products into various parts of the cell, which would compete with efficient flushing of the cell.

The nitric acid product from the OH + NO<sub>2</sub> photolysis experiments provides a strong spectroscopic measure of “photolysis products.” We therefore measured the flush rate directly by monitoring the nitric acid signal as a function of the YAG – Excimer delay time. Figure 6.7 shows data taken at 600 torr and a calculated flush time of 80 ms.

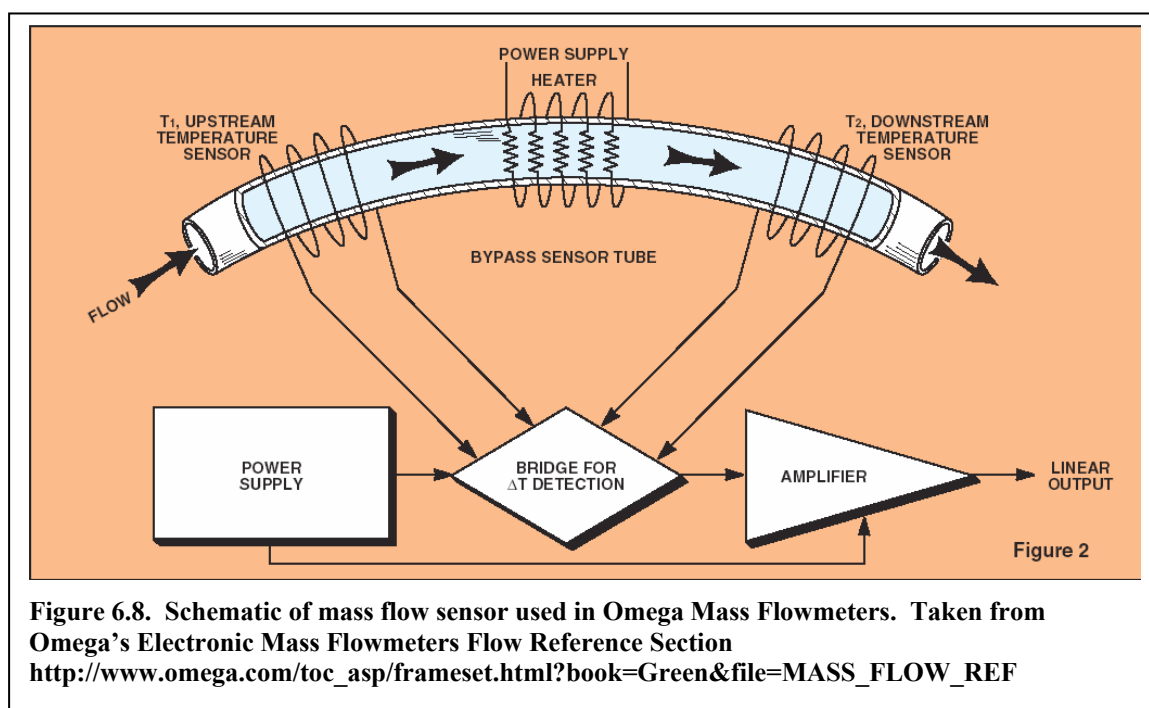


We see that the initial decrease in nitric acid signal exceeds that predicted by flushing alone, i.e., far less than half the initial nitric acid remains in the probe region 40 ms after the initial photolysis. Presumably this can be explained by diffusion of nitric acid out of the region of the cell being probed by the IR-CRDS. After this initial rapid decay, the signal decays much slower and asymptotes to 1.3% of the signal at 500  $\mu$ s. Given the notoriety of nitric acid as a very sticky molecule, this remaining signal may more reflect the desorption of nitric acid stuck to the walls of the flow cell than poor flushing of photolysis volume.

Regardless, for our purposes the 1.5% signal at the calculated flush time of 80 ms reflects essentially complete flushing of the photolysis volume. This level of signal was used to determine a minimum flush time (the calculated flush time needed to reduce the signal to 1.5% its initial value at the next excimer shot) at a few different pressures. While this time at 400 torr was about the same as that at 600 torr (88 mS), at 200 torr a faster flush time of about 65 ms was needed. This implies that at lower pressures, diffusion may indeed begin to play an important role and the “factor of two” rule may once again apply. Fortunately, at lower pressures faster flush times are readily achieved.

## 6.4 Mass Flow Transducers

Mass flow transducers (flowmeters) are a critical component of the flow-cell experiments described in this thesis. They enable us to control and precisely know the concentrations of all gases in the cell. This information is critical for any kinetics simulations or cross-section measurements. As implied by their formal name, flowmeters determine mass flow of gas through their sensor. This is accomplished by detecting the heat transferred by a flowing gas, which is directly proportional to the mass flow of the gas. A diagram of the sensors used in Omega flowmeters is shown in Figure 6.8.



The temperature difference between the upstream and downstream temperature sensors is converted to a voltage that is linearly related to the mass flow. In order to interpret this voltage, the sensitivity of the flowmeter, given in sccm/volt, must be known

(sccm = standard cubic centimeter =  $1\text{cm}^3$  of gas at  $70^\circ\text{F}$  and 1 atm). Because the sensor relies on the thermal conductivity of the gas, the sensitivity is gas specific, so the calibration changes when the gas is changed. The calibration for a new gas can be calculated using conversion tables provided in the manuals for each flowmeter.

Sensitivities are provided with any new flowmeter, but should be calibrated upon arrival and re-calibrated periodically. This is accomplished by flowing through calibrated volumes, specifically those included in the calibration kit borrowed from the Sander group at JPL. This kit includes several volumetric cylinders (10, 100, and  $1000\text{ cm}^3$ ) each with a ground glass joint on one end. This joint couples the cylinder to a specialty piece of glassware that introduces soap bubbles to the upstream end of the cylinder. The flow rate is then measured by measuring the time it takes for the soap bubbles to displace the volume of the cylinder. Following corrections for the temperature, pressure, and vapor pressure of water, the flow in standard cubic centimeters is determined and can be plotted as a function of the voltage readout of the flowmeter.

The flowmeters in 17 Noyes were originally all manufactured by Edwards. These all had corrosion-resistant stainless steel bodies, bipolar electrical connections (although of a rather inconvenient design) and were generally robust. Unfortunately, as time has worn on, the sensors in the Edwards flowmeters have begun to go bad. Usually this is a gradually accelerating process of decreasing sensitivity to flow (an increase in the sccm/volt measured when calibrating). This is a serious problem because Edwards left the flowmeter business years ago and, when they left, apparently did not sell their extra sensors or the rights to make them to any other company. As a result, once a flowmeter sensor goes bad, the flowmeter is no longer useable and must be replaced.

So far, the flowmeters that have gone bad have tended to be those for higher flow used for dilution or purge flows of inert gas. As a result, they have been replaced with inexpensive brass-body flowmeters from Omega. These flowmeters must be used *with inert gas only*. Under ideal conditions, these flowmeters seem to work fine. Their sensitivities do not seem to vary between calibrations and the calibration curves are linear, yielding uncertainties in the flow on the order of 0.5%.

However, problems with these Omega flowmeters do exist. First, the power supply is of a positive voltage only. As a result, the flowmeters cannot read any voltage below 0.0 V. This can be and has been a problem when the zero-flow offset is such that the voltage at no flow is not a positive value. When this occurs, there is a range of low flows that will all read zero. In a calibration curve, this is evidenced by a significant positive y-intercept. As a result, it is important to check that the zero-flow reading from the Omega flowmeters is above zero (it is wise to check the value before and after an experiment to account for drift), and then subtract this value from all readings that day.

The more serious issue with the Omega flowmeters stems from the fragility of their electronics. The first time the Omega flowmeters broke, it was clearly my fault. I had been making changes to the power supply and readout box and accidentally reconnected the positive and negative leads backwards. This apparently fried all three Omega flowmeters. It is interesting to note that this did not seem to affect the Edwards flowmeters at all. This does not necessarily imply an inherent problem with the Omega flowmeters, but a better design would have included a fuse or other safety device that would have protected the sensor in case of lab idiot.

The second destruction of flowmeter confirms this. It is generally advised that before you connect or disconnect a flowmeter you turn its power supply off. I would again like to point out that the Edwards flowmeters were connected and disconnected with the power on for years before I joined the group without any drastic consequences. As a result of the shorted electronics mentioned above, I have been very careful to power down the flowmeters before performing any work on them. A recent addition to the lab (who will remain unnamed) changed the gas connections to the flowmeters with the power on. This was just a plumbing job, with no changes to the electronics. After the plumbing was done, one of the Omega flowmeters was broken. Presumably, something touched its nine-pin connector during the job and caused a short. While again this could have been prevented by powering down the flowmeters, relying on these Omega flowmeters that are so prone to breaking is not ideal (in this latter case, we were able to convince them to replace the unit for free, but not without nearly a month of downtime). As a result, I advise switching to a new company when next we need a new flowmeter.

The flowmeter-readout-DIO system is a bit messy, which I believe is a large part of the slow response time of the flowmeter readouts (settling time after changing flow of about ten seconds). The setup could definitely be improved.

**WARNINGS:**

- **With Omega flowmeters, flow ONLY INERT GAS.**
- **Turn power to flowmeters off (power strip mounted to laser table cover) before any work on flowmeters.**
- **Always check calibrations against the previous value to check for sensors that are beginning to fail.**

## 7 Appendix C: CRDS Simulation Programs for Matlab

### 7.1 Introduction

I cannot give Gautham Nair enough credit for writing these. He did all the legwork on designing the program, wrote a version of the program for C++ and then wrote the original version of these fitting programs. I have made adjustments to the code to for convenience and flexibility, but Gautham should definitely be considered the author of the program. Many thanks also to Kana Takematsu for taking these programs through the motions and helping with the documentation included in this appendix.

It should be noted that after Gautham left for some lesser school in Massachusetts, he wrote some of the programs on a different version of Matlab and there was a small compatibility issue. I worked with Matlab 7.0. To get these programs to work on other versions of Matlab it may be necessary to replace the comma separating output variables of a function with a space i.e. change

```
function [ringspec,simplespec]=
```

to

```
function [ringspec simplespec]=
```

#### 7.1.1 Motivation

As described in Chapter 2, pulsed CRDS measurements of spectra with narrow features can have significant errors in the form of incorrect lineshapes and observed integrated absorbances below the true value. These errors stem from fitting observed multi-exponential decays with a single exponential function to extract the decay lifetime

$\tau$ . The general goal of these programs is to simulate the expected CRDS signal for a given set of apparatus conditions if the underlying high-resolution spectrum is known. This high resolution spectrum is adjusted by pressure broadening and application of scale factors to take into account species concentration and convert the spectrum from absorbance units to  $1/\tau$ .

This spectrum is then convolved with the laser profile to generate the simulated ringdown spectra. At each point in the simulated spectrum, a simulated ringdown decay is produced by summing the individual decays at each frequency weighted by the laser profile,  $\sum_i \frac{\alpha_i}{\tau_i} e^{-t/\tau_i}$ , where  $\alpha$  is the normalized weighting function for the laser profile. The simulated ringdown decay is then fit with a single exponential function to generate the “experimental” ringdown decay lifetime ( $1/\tau'$ ). This is then repeated for all frequencies in the simulated spectrum. The integrated absorption of the new spectrum and the convolved spectrum without re-fitting the decay,  $\sum_i \frac{\alpha_i}{\tau_i}$ , can be compared to derive the error in the CRDS spectrum.

The magnitude of the CRDS errors and their sensitivity to various parameters can then be explored. Because there are many parameters which we might be interested in varying systematically, there are several versions of the program each designed to systematically vary an individual parameter. In theory these various programs could be combined into one generalized program, but so far I have found this to be unnecessary.

### 7.1.2 Using MATLAB:

Some general tips for running routines in Matlab. The program files must be contained in the Current Directory shown in Matlab. All saved files will also automatically go to the Current Directory. You can specify any output names you want. Inputs that are arrays or matrices must be pre-existing named items in the Matlab workspace. To run a routine, such as Lorentzbroaden.m broadening the high-resolution spectrum “inputspectrumname” to  $.05 \text{ cm}^{-1}$ , you would just type into the command line

```
outputspectrumname = Lorentzbroaden(0.05, 2.0, inputspectrumname);
```

and press enter. The semicolon at the end ensures that the output spectrum is not printed to the Command Window. When the program is finished, the new matrix “outputspectrumname” will appear in the Workspace.

WARNING: If you run the program again and do not change the output name, it will be written over without any prompt to warn you!

Comments can be added to any routine by beginning the line with “%”.

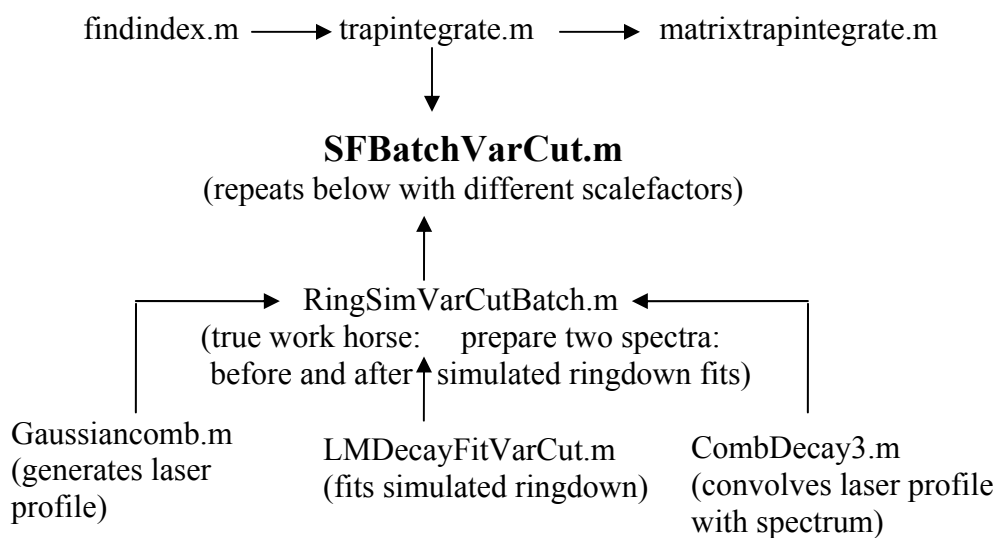
To save any output matrix to a text file for manipulation in another program, use “save savefilename.out matrixname –ASCII”

When trying to go through the program, it is helpful to generate a fake matrix to manipulate. Just define a matrix (“matrix=...” or [starting point: interval dist: finishing point].) The matrix will appear in the Workspace. If you want to manipulate it, just double click on it. To quickly generate an array (such as a column array of scalefactors for use in SFBatchFixCut.m) you can use

```
newarrayname = (startnumber:stepsize:endnumber)';
```

The apostrophe at the end rotates the array from a row to a column. If you want column *i* of matrix, just write `matrixname(:,i)`. If you want a row, write `matrixname(i,:)`. If you want to manipulate any matrix (change/add/delete elements), just double click on it.

A flow diagram for the “SFBatchVarCut.m” top-level program to illustrate which programs are interconnected is shown here. The programs are highly modular so that changing and debugging programs is quite simple, even for a novice like me. An arrow indicates a flow of outputs. For example, `RingSimVarCutBatch.m` calls three different sub-routines, “`Gaussiancomb.m`”, “`LMDecayFitVarCut.m`” and “`CombDecay3.m`”. It then uses the information gathered from those sub-routines and sends outputs to “`SFBatchVarCut.m`”. It is important when running a program in Matlab that all needed sub-routines are contained in the Current Directory.



## 7.2 Program Documentation

Programs are shown below in single-spaced text. If using higher-level programs, sub-routines need to be saved with the titles shown in quotation marks.

### 7.2.1 Common Inputs

**abspectrum** = data spectrum used for simulation. Usually the output of

Lorentzbroaden.m

**times** = 1D column array specifying the time axis of the ringdowns. Should reflect the number of points and sample rate of the experiment you are simulating.

**background** = background value for  $1/\tau$ . Should be in  $s^{-1}$ .

**xi,xf** = range of simulated spectrum. (xi-regionwidth) and (xf-regionwidth) should not exceed the range of abspectrum.

**scannedwavenumbers** = 1D column array of frequencies you want in the output spectrum. This is where you would define the stepsize of the spectrum. Could be used to eliminate xi and xf with a short re-program.

**regionwidth** = range in  $cm^{-1}$  (or whatever units your spectra are in) over which the laser profile will be used to calculate the simulated ringdown at each point.  $2 * laserfwhm$  was sufficient in HNO<sub>3</sub>.

**laserfwhm** = laserfwhm in  $cm^{-1}$  (or whatever units your spectra are in). Treats laser profile as Gaussian (for most simulations assumed to be  $1.0 cm^{-1}$ ). Actually treats profile as discrete spikes with spacing defined by ...

**modespace** = spacing of modes for Gaussian laser profile. Generally assumed to be  $0.00666 cm^{-1}$  we expect from the YAG cavity.

## 7.2.2 “Lorentzbroaden.m”

DESCRIPTION: This program is designed to take a high resolution, Doppler-limited spectrum and convolve it with a Lorentzian lineshape to simulate pressure-broadening.

Reminder: Lorentzian 
$$\frac{1}{\pi} \frac{\frac{1}{2}\Gamma}{(x-x_0)^2 + (\frac{1}{2}\Gamma)^2}$$

For nitric acid, we found that having regionwidth=2\*fwhm was insufficient. If you can spare points at the edge of your spectrum, you should try for at least 4\*fwhm.

### **%Inputs**

```
%fwhm=fwhm of Lorentzian profile you are convolving
%regionwidth=total width over which each spectral point will be "spread".
%spectrum=2D matrix containing data spectrum to convolve. Can be imported
%using Matlabs "Import Data" routine. First column must be x-axis
%(frequency units must match fwhm and regionwidth)
% second column can be any arbitrary frequency units.
function broadspec=Lorentzbroaden(fwhm, regionwidth, spectrum);
specspacing=spectrum(2,1)-spectrum(1,1);
convpoints=round(regionwidth/(2*specspacing));
```

### **%this initiates the matrices used in the calculation**

```
Npoints=size(spectrum,1);
broadspec=2*ones(Npoints-2*convpoints,2);
```

### **%Here is the meat of it. If you wanted to change this to use a different shape you would change the second line.**

```
%Motivation for loop: we are going to take each point of the spectrum. Each point is
%going to be treated like a Lorentzian i.e. the intensity assigned to each point is going to
%be redistributed as a Lorentzian. The transformed functions are then going to be
%summed.
```

```
for i=(convpoints+1):(Npoints-convpoints)
    lorweights=1./((spectrum((i-convpoints):(i+convpoints),1)-spectrum(i,1)).^2 ...
    +(fwhm/2)^2);
    lorweights=lorweights/sum(lorweights);
    broadspec(i-convpoints,1)=spectrum(i,1);
    broadspec(i-convpoints,2)=sum(spectrum((i-convpoints):(i+convpoints),2).*lorweights);
end
```

### 7.2.3 “trapintegrate.m”

DESCRIPTION: Used to integrate spectra. Built into the Batch programs below, but can be used for any spectrum in the Workspace that is a 2D matrix with frequency in column 1 and absorbance in column 2. Fairly self explanatory.

```
function trapintegral = trapintegrate(xi,xf,spectrum);
ni = findindex (xi,spectrum); nf = findindex (xf,spectrum);
trapintegral=0.0;
trapintegral=sum(spectrum(ni:(nf-1),2).*(spectrum((ni+1):nf,1)-spectrum(ni:(nf-1),1)));
```

### 7.2.4 “matrixtrapintegrate.m”

DESCRIPTION: Can be used to get the integrals of multiple spectra contained in a 2D matrix where the columns are spectra (such as the outputs from the Batch programs below). **xi** and **xf** should be entered as numbers, **wavelengths** should be a column array such as “scannedwavenumbers” described above, and **spectraonly** should be a matrix with each column as the absorbance points corresponding to the frequencies in “wavelengths”.

```
function trapintegrals=matrixtrapintegrate(xi,xf,wavelengths,spectraonly)
trapintegrals=[];
for i=1:size(spectraonly,2)
    trapintegrals=[trapintegrals trapintegrate(xi,xf,[wavelengths,spectraonly(:,i)])];
end
```

### 7.2.5 “Gaussiancomb.m”

DESCRIPTION: Generates a Gaussian shape for use in simulation programs using “laserfwhm”, “regionwidth”, and “modespace” to describe the laser profile. The “combpattern” output is 2D array describing a Gaussian with 0 as the center point.

```
function combpattern = Gaussiancomb(laserfwhm,regionwidthcm,modespace);

lasersigma=laserfwhm/sqrt(8*log(2));
temp1=0:modespace:regionwidthcm/2;
temp2=-temp1;
temp2(1)=[];
combpoints=[fliplr(temp2) temp1]';
combintensities=exp(-(combpoints.^2)/(2*lasersigma^2));
combpattern=[combpoints combintensities];
```

### 7.2.6 “findindex.m”

DESCRIPTION: Simple program called to give the index number.

```
function n=findindex(x,spectrum)
n=interp1(spectrum(:,1),(1:size(spectrum,1))',x,'nearest');
```

### 7.2.7 “SFBatchFixCut.m” and “SFBatchVarCut.m”

DESCRIPTION: To be used when you want to run several simulations at various “concentrations” (scalefactors). Shown is the program designed to do the ringdown fits cutting a fixed number of points at the start of the simulated ringdown,

SFBatchFixCut.m. The program for cutting a fraction of a ringdown for each trace,

SFBatchVarCut.m, is identical but calls “RingSimVarCutBatch.m” in the for-loop.

#### UNIQUE INPUTS:

**scalefactors** = 1D column array containing all scalefactors you want used.

NOTE: later in the RingSimFixedCutBatch, the scales factor is multiplied by the arbitrary number  $6.024 \times 10^{18}$ . If working with known absorbances, it should be possible to change this number so that scaled absorbances represent the expected signal rather than its current arbitrary value.

```
function [ringspecs,simplespecs,integrals,Summary] = SFBatchFixCut (scalefactors, xi,
xf, abspectrum, background, scannedwavenumbers, times, laserfwhm, regionwidth,
modespace);
```

```
pringtemp=[];
rringtemp=[];
psimtemp=[];
rsimtemp=[];
ringspecs=[];
simplespecs=[];
Summary=[];
integrals=[];
Npoints=length(scannedwavenumbers);
%length = # of rows in matrix
```

```
%this iterates RingSimFixedCutBatch for each scalefactor
```

```
for i=1:length(scalefactors)
```

```
  [ringspec,simplespec]=RingSimFixedCutBatch(laserfwhm, regionwidth, modespace,
times, scannedwavenumbers, background, scalefactors(i), abspectrum);
```

```

%see later pages for RingSimFixedCutBatch.m.
ringspecs=[ringspecs ringspec];
%[elements1 elements2] combines the elements into one large array
simplespecs=[simplespecs simplespec];
integrals=[integrals [trapintegrate(xi,xf, [scannedwavenumbers ringspec]);...
    trapintegrate(xi,xf, [scannedwavenumbers simplespec])]];
%notice the “;” between the trapintegrates. This puts the results in two separate rows
%this calculates the integrated absorption for ringsepc and simplespec.
pringtemp=[pringtemp ringspec(1)];
rringtemp=[rringtemp ringspec(Npoints)];
psimtemp=[psimtemp simplespec(1)];
rsimtemp=[rsimtemp simplespec(Npoints)];
end

%this creates a matrix with columns containing the simulated spectrum
%integral, the integral of the spectrum with no CRDS error, and the first
%and last point in the spectra for both the simulation and with no CRDS
%error (critical for trying to evaluate the error outside the bounds of
%your simulation).
Summary=[integrals' pringtemp' psimtemp' rringtemp' rsimtemp'];

```

### 7.2.8 “ScalefactorBatchCustom.m”

DESCRIPTION: This is the same as SFBatchVarCut.m but it is designed so that any arbitrary laser profile can be used (above routines used Gaussian profile). The normalized laser profile needs to be a pre-existing 2D matrix with the first column as  $\Delta(\text{frequency})$  with the center of the profile as 0 and the second column the normalized intensity at each value of  $\Delta(\text{frequency})$ .

```
function [ringspecs, simplespecs, integrals, Summary] = ScalefactorBatch (scalefactors,
xi, xf, absspectrum, background, scannedwavenumbers, times, laserprofile);
%in comparison with SFBatchFixCut, laserprofile has replaced inputs laserfwhm,
%regionwidth and modespace.
```

```
pringtemp=[];
rringtemp=[];
psimtemp=[];
rsimtemp=[];
ringspecs=[];
simplespecs=[];
Summary=[];
integrals=[];
Npoints=length(scannedwavenumbers);
```

```
for i=1:length(scalefactors)
    [ringspec, simplespec]=RingdownSimCustom(laserprofile, times,
scannedwavenumbers, background, scalefactors(i), absspectrum);
%see later pages for RingdownSimCustom.m
    ringspecs=[ringspecs ringspec];
    simplespecs=[simplespecs simplespec];
    integrals=[integrals [trapintegrate(xi,xf, [scannedwavenumbers ringspec]);...
        trapintegrate(xi,xf, [scannedwavenumbers simplespec])]];
    pringtemp=[pringtemp ringspec(1)];
    rringtemp=[rringtemp ringspec(Npoints)];
    psimtemp=[psimtemp simplespec(1)];
    rsimtemp=[rsimtemp simplespec(Npoints)];
end
```

```
Summary=[integrals' pringtemp' psimtemp' rringtemp' rsimtemp'];
```

### 7.2.9 “fwhmBatch.m”

DESCRIPTION: Very similar to SFBatch programs above, but you can run a batch of various values of laser fwhm (**laserfwhms**) instead of scalefactors. **widthfactor** is a number which will be multiplied by each laser fwhm to define the “regionwidth” described above.

**function** [ringspecs,simplespecs,integrals,Summary] = fwhmBatch (scalefactor, xi, xf, absspectrum, background, scannedwavenumbers, times, laserfwhms, widthfactor, modespace);

```
pringtemp=[];
rringtemp=[];
psimtemp=[];
rsimtemp=[];
ringspecs=[];
simplespecs=[];
Summary=[];
integrals=[];
Npoints=length(scannedwavenumbers);
```

```
for i=1:length(laserfwhms)
    [ringspec,simplespec]=RingdownSim3(laserfwhms(i), laserfwhms(i)*widthfactor,
    modespace, times, scannedwavenumbers, background, scalefactor, absspectrum);
    ringspecs=[ringspecs ringspec];
    simplespecs=[simplespecs simplespec];
    integrals=[integrals [trapintegrate(xi,xf, [scannedwavenumbers ringspec]);...
        trapintegrate(xi,xf, [scannedwavenumbers simplespec])]];
    pringtemp=[pringtemp ringspec(1)];
    rringtemp=[rringtemp ringspec(Npoints)];
    psimtemp=[psimtemp simplespec(1)];
    rsimtemp=[rsimtemp simplespec(Npoints)];
end
```

```
Summary=[integrals' pringtemp' psimtemp' rringtemp' rsimtemp'];
```

## 7.2.10 “RingSimFixedCutBatch.m” and “RingSimVarCutBatch.m”

DESCRIPTION: Calculates the simulated CRDS spectrum and convolved spectrum for each scalefactor. Shown is RingSimFixedCutBatch.m which uses fits cutting a fixed time period at the start of each ringdown. RingSimVarCutBatch.m uses fits cutting a fraction of a lifetime at the start of each ringdown, and replaces LMdecayfitmodified.m with LMDecayFitVariableCut.m

```
function [ringspec,simplespec]=RingSimFixedCutBatch(laserfwhm, regionwidth,
modespace, times, scannedwavenumbers, background, scalefactor, absspectrum)
combpattern=Gaussiancomb(laserfwhm,regionwidth,modespace);
Nscans=size(scalefactor,1);
Npoints=size(scannedwavenumbers,1);
ringspec=zeros(Npoints,Nscans);
%zeros(m,n) generates m x n matrix with all elements = 0
simplespec=zeros(Npoints,Nscans);
tempdecay=zeros(size(times));
%if zeros(m), creates m x m matrix
simpleinvlifetime=0.0;
tempfitparam=[];

%This does the work of calling Combdecay3.m and LMDecayfitmodified.m for each
%point in the simulated spectra and compiling those numbers for export to
%SFBatchFixCut.m.
for j=1:Nscans
    invlifetimes=[absspectrum(:,1) background + scalefactor(j)* 6.024*10^8*
absspectrum(:,2)];
%creates two column matrix with x and adjusted y. 6.024*10^8 is arbitrary
for i=1:Npoints
    [tempdecay simpleinvlifetime] = CombDecay3 (scannedwavenumbers(i), times,
combpattern, invlifetimes);
%will discuss CombDecay3.m later
    tempfitparam = LMdecayfitmodified (times, tempdecay, tempdecay(1),
simpleinvlifetime);
%will discuss LMdecayfitmodified.m later
    ringspec(i,j)=tempfitparam(2)-background;
    simplespec(i,j)=simpleinvlifetime-background;
%These two outputs will later be called for in the batch files and combined with the
%scanned wavelengths to reconstruct the spectra.
end
end
```

### 7.2.11 “RingdownSim3.m”

DESCRIPTION: This is the first version of the RingdownSim program that is designed for a single set of inputs. The version here uses LMDecayfit.m which fits the full simulated ringdowns. It could easily be modified to use either of the other versions of LMdecayfit by replacing it with the desired version below.

```
function [ringspec,simplespec]=RingdownSim(laserfwhm, regionwidth, modespace,
times, scannedwavenumbers, background, scalefactor, absspectrum)
combpattern=Gaussiancomb(laserfwhm,regionwidth,modespace);
Npoints=size(scannedwavenumbers,1);
ringspec=zeros(Npoints,1);
simplespec=zeros(Npoints,1);
tempdecay=zeros(size(times));
simpleinvlifetime=0.0;
tempfitparam=[];
invlifetimes=[absspectrum(:,1) background+scalefactor*6.024*10^8*absspectrum(:,2)];

for i=1:Npoints
    [tempdecay
simpleinvlifetime]=CombDecay3(scannedwavenumbers(i),times,combpattern,
invlifetimes);
    tempfitparam=LMdecayfit(times,tempdecay,tempdecay(1),simpleinvlifetime);
    ringspec(i)=tempfitparam(2)-background;
    simplespec(i)=simpleinvlifetime-background;
end
```

### 7.2.12 “RingdownSimCustom.m”

DESCRIPTION: This is the version of RingdownSim that can use an arbitrary user-defined laser profile. Otherwise the same as other versions. Currently uses “LMdecayfitVariableCut.m” but could be changed to the Fixcut version.

```
function [ringspec,simplespec]=RingdownSim(laserprofile, times, scannedwavenumbers,
background, scalefactor, abspectrum)
Npoints=size(scannedwavenumbers,1);
ringspec=zeros(Npoints,1);
simplespec=zeros(Npoints,1);
tempdecay=zeros(size(times));
simpleinvlifetime=0.0;
tempfitparam=[];
invlifetimes=[abspectrum(:,1) background+scalefactor*6.024*10^8*abspectrum(:,2)];

for i=1:Npoints
    [tempdecay simpleinvlifetime] = CombDecay3 (scannedwavenumbers(i), times,
laserprofile, invlifetimes);
    tempfitparam = LMdecayfitVariableCut (times, tempdecay, tempdecay(1),
simpleinvlifetime);
    ringspec(i)=tempfitparam(2)-background;
    simplespec(i)=simpleinvlifetime-background;
end
```

### 7.2.13 “Combdecay3.m”

DESCRIPTION: This creates the simulated ringdown decays that will be fit later. It also calculates the signal at each point that would be seen by simply convolving the spectrum with combpattern. This is called by the RingSim programs. Many of the inputs here will be called by index in the main programs.

UNIQUE INPUTS: **cavityinvlifetimes** contains the inverse ringdown lifetimes for given wavenumber input light. First column is wavenumber, second is inverse lifetime ( $1/\tau$ ).

**function** [decay,simpleavg] = CombDecay (centerwavenumber, times, combpattern, cavityinvlifetimes);

%centerwavenumber is a number (the frequency at which the laser is centered)  
 %times is a 1d array of desired times to sample the decay (i.e. the  
 %oscilloscope decay trace data)  
 %combpattern is a 2d array. It is a simulation of the frequency spectr  
 %um of the laser shot, assuming wavenumber 0 is the center position.  
 %The first column is wavenumbers and the second  
 %column indicates the laser intensity at the corresponding wavenumber.  
 %cavityinvlifetimes contains the inverse ringdown lifetimes for given wavenumber  
 %input light. First column is wavenumber, second is inverse ( $1/e$ ) lifetime.  
 %decay is the output decay signal and simpleavg is the  
 %cavity inverse lifetime that would be obtained by simply convolving  
 %the input spectrum with the comb pattern.

timesize = size (times,1);  
 decay = zeros (timesize,1);  
 combsize = size (combpattern,1);  
 combinvlifetimes = zeros (combsize,1);  
 combinvlifetimes = interp1 (cavityinvlifetimes(:,1), cavityinvlifetimes(:,2),  
 combpattern(:,1)+centerwavenumber, 'linear',NaN);  
 %interp1 is a interpolation (table lookup) function contained in Matlab.  
 %YI = interp1(X,Y,XI). Sometimes X is left out. This assumes that X=1:N. Note XI  
 %stands for x interval i.e. if X = 0:10, then XI=0:.25:10.  
 %Sometimes, after XI, a “method” is chosen in which the interpolation is done. The  
 %default is linear interpolation. Sometimes after ‘method,’ the ‘extrap” option can be

%stated. This chooses a method for extrapolating any elements of XI outside the interval %spanned by X. Alternatively, "EXTRAPVAL" replaces these values with %EXTRAPVAL. NaN and 0 are often used for this number.

%Aside: Interpolation: constructing new data points from discrete set of known data  
% Extrapolation: find value of function at point x which is outside  $x_k$  of function

for i=1:timesize

    decay(i)=sum(combpattern(:,2).\*exp(-times(i)\*combinvlifetimes));

end

simpleavg=sum(combpattern(:,2).\*combinvlifetimes)/sum(combpattern(:,2));

%Notice that the combpattern is normalized here, as the Gaussian was not normalized

%in the subroutine. The decays generated above will be sent into LMDecayFit programs.

%The decay does not need to be normalized as it is just going to be refit later.

%Multiplying by a constant for normalization will not change the ringdown time.

### 7.2.14 “LMDecayFitModified.m”

DESCRIPTION: This actually fits the simulated decay traces using the Levenberg-Marquardt algorithm. I believe the fitting algorithm was taken from Numerical Recipes, but I’m not sure. This particular iteration has a fixed amount of time cut from the beginning of the trace before it is fit.

INPUTS: **fulltimes** is the decay time points (same as **times** from above).

**fulldecsignal** is the decay signal as generated by CombDecay3.m

**inita** initial guess for the amplitude (generally taken as the first point in “fulldecsignal”

**initb** is the initial guess for the lifetime (generally taken from the “simpleinvlifetime” output of CombDecay3.m).

```
function fitparam=LMdecayfit(fulltimes, fulldecsignal, inita, initb)
```

```
%This part makes the fit neglect times below a certain threshold
```

```
%This is the threshold value, in whatever units your times are in:
```

```
%Keep negative if you want it to work just as before.
```

```
%Must be changed manually here (does not read from higher-level programs).
```

```
tbegin=16e-8;
```

```
%This is the code that takes care of the cutting.
```

```
tmask=fulltimes>tbegin;
```

```
times=fulltimes(tmask);
```

```
decsignal=fulldecsignal(tmask);
```

```
% The rest of this is fits the remaining points.
```

```
chisq=0.0;
```

```
ochisq=0.0;
```

```
a=0.0;
```

```
oa=0.0;
```

```
da=0.0;
```

```
b=0.0;
```

```
ob=0.0;
```

```
db=0.0;
```

```
lambda=0.001;
```

```
beta=zeros(2,1);
```

```

alpha=zeros(2,2);
convergedflag=1;
convergecrit=0.005;
Niterations=1;
Nmax=50;
oa=inita;
ob=initb;
a=oa;
b=ob;
ochisq=sum((decsignal-oa*exp(-ob*times)).^2);

while convergedflag&&(Niterations<Nmax)
    beta=zeros(2,1);
    alpha=zeros(2,2);
    exptemp=exp(-ob*times);
    beta(1)=sum((decsignal-oa*exptemp).*exptemp);
    beta(2)=sum(-oa*times.*(decsignal-oa*exptemp).*exptemp);
    alpha(1,1)=sum(exptemp.^2)*(1+lambda);
    alpha(1,2)=sum(-oa*times.*exptemp.^2);
    alpha(2,1)=alpha(1,2);
    alpha(2,2)=sum(oa^2*times.*times.*exptemp.^2)*(1+lambda);
    da=(alpha(2,2)*beta(1)-alpha(1,2)*beta(2))/(alpha(1,1)*alpha(2,2)-
alpha(1,2)*alpha(2,1));
    db=(alpha(1,1)*beta(2)-alpha(2,1)*beta(1))/(alpha(1,1)*alpha(2,2)-
alpha(1,2)*alpha(2,1));
    a=oa+da;
    b=ob+db;
    chisq=sum((decsignal-a*exp(-b*times)).^2);
    if chisq>ochisq
        lambda=lambda*10;
    else
        lambda=lambda*0.1;
        oa=a;
        ob=b;
        if ((ochisq-chisq)<(chisq*convergecrit))||chisq==0
            convergedflag=0;
        end
        ochisq=chisq;
    end
    Niterations=Niterations+1;
end

fitparam=[a ; b ; Niterations;ochisq];
%Output file gives a = amplitude, b = exponent factor, number of iterations that were
%used in the Levenberg-Marquardt algorithm, and the chi^2 value of the fit.

```

### 7.2.15 “LMDecayFitVariableCut.m”

DESCRIPTION: This is identical to “LMDecayFitModified.m” described above, but a fraction of the decay is cut instead of a fixed amount.

```
function fitparam = LMdecayfitVarCut(fulltimes, fulldecsignal, inita, initb)
```

```
%this makes an initial fit, in order to get a guess for the lifetime
tfitparam=LMdecayfit(fulltimes, fulldecsignal, inita, initb);
%This part makes the fit neglect times below a certain threshold
tempa=0.0;
tempb=0.0;
tempa=tfitparam(1);
tempb=tfitparam(2);
%This is the threshold value, in whatever units your times are in:
%Keep negative if you want it to work with no cut. Currently set to cut
%half of a lifetime. Needs to be changed manually on the following
%line.
tbegin=0.5*(1/tempb);

%This is the code that takes care of the cutting
tmask=fulltimes>tbegin;
times=fulltimes(tmask);
decsignal=fulldecsignal(tmask);
% This is the end of this part, the rest of the function is as in LMDecayFitModified.m
```

### 7.2.16 “SingledecayVarfitRes.m”/ “SingledecayFixCutRes.m”

DESCRIPTION: These programs are designed to run at a single frequency and allow you to look at the actual ringdowns. The output **decays** is a 3-column matrix with the first column the simulated ringdown, the second column the fit to the simulated ringdown and the third column the residual. Shown in the Varfit version, FixCut is the same but with the LMdecayfit program changed.

```
function [decays,ringinvT,simpleinvT] = SingledecayVarfitRes (laserfwhm, regionwidth,
modespace, times,wavenumber, background, scalefactor, abspectrum)
```

```
combpattern=Gaussiancomb(laserfwhm,regionwidth,modespace);
decays=zeros(size(times,1),3);
```

```
[decays(:,1),simpleinvT] = CombDecay3(wavenumber,times,combpattern, ...
[abspectrum(:,1) background+ scalefactor* 6.024*10^8* abspectrum(:,2)]);
fitparam= LMdecayfitVariableCut (times, decays(:,1), decays(1,1), simpleinvT);
decays(:,2)=fitparam(1)*exp(-fitparam(2)*times);
decays(:,3)=(decays(:,1)-decays(:,2));
ringinvT=fitparam(2)-background;
simpleinvT=simpleinvT-background;
```